

# Nucleotide metabolism in cancer cells fuels a UDP-driven macrophage cross-talk, promoting immunosuppression and immunotherapy resistance

Received: 5 January 2024

Accepted: 23 April 2024

Published online: 06 June 2024

 Check for updates

A list of authors and their affiliations appears at the end of the paper

Many individuals with cancer are resistant to immunotherapies. Here, we identify the gene encoding the pyrimidine salvage pathway enzyme cytidine deaminase (CDA) among the top upregulated metabolic genes in several immunotherapy-resistant tumors. We show that CDA in cancer cells contributes to the uridine diphosphate (UDP) pool. Extracellular UDP hijacks immunosuppressive tumor-associated macrophages (TAMs) through its receptor P2Y<sub>6</sub>. Pharmacologic or genetic inhibition of CDA in cancer cells (or P2Y<sub>6</sub> in TAMs) disrupts TAM-mediated immunosuppression, promoting cytotoxic T cell entry and susceptibility to anti-programmed cell death protein 1 (anti-PD-1) treatment in resistant pancreatic ductal adenocarcinoma (PDAC) and melanoma models. Conversely, CDA overexpression in CDA-depleted PDACs or anti-PD-1-responsive colorectal tumors or systemic UDP administration (re)establishes resistance. In individuals with PDAC, high CDA levels in cancer cells correlate with increased TAMs, lower cytotoxic T cells and possibly anti-PD-1 resistance. In a pan-cancer single-cell atlas, *CDA*<sup>high</sup> cancer cells match with T cell cytotoxicity dysfunction and *P2RY6*<sup>high</sup> TAMs. Overall, we suggest CDA and P2Y<sub>6</sub> as potential targets for cancer immunotherapy.

Immunotherapy, including adoptive T cell transfer, cancer vaccines and immune checkpoint blockade (ICB), represents a promising treatment option for individuals with cancer<sup>1</sup>. For instance, programmed cell death protein 1 receptor (PD-1) is an immune checkpoint protein expressed on the cell surface of T cells. By binding its cognate ligand (PD-L1), PD-1 turns down an uncontrolled T cell response by modulating T cell antigen receptor (TCR) signaling. In tumors, cancer cells hijack this pathway by overexpressing PD-L1. Hence, the therapeutic potential of antibodies to PD-1 has been intensely investigated<sup>2</sup>.

Despite the high response rates with prolonged survival in subsets of individuals with melanoma<sup>3</sup>, lung<sup>4</sup> and renal cancer<sup>5</sup>, ICB failed to show clinical benefit in several other tumors, such as the majority of mismatch repair-proficient colorectal cancers<sup>6</sup> and pancreatic ductal adenocarcinoma (PDAC)<sup>7</sup>.

PDAC is one of the most aggressive and lethal cancers, with an overall 5-year survival rate of 9%. The projected doubling of PDAC incidence by 2030 would make it the second leading cause of cancer-related death after lung cancer. The majority of individuals present at advanced stages with distant organ metastases and/or locoregional extension, resulting in less than 20% of individuals being eligible for resection at the time of diagnosis<sup>8</sup>. Most therapies, including ICB, are not effective<sup>7</sup>, and the majority of individuals who undergo surgery ultimately relapse<sup>9</sup>. Thus, there is urgent need for treatments that are applicable to most individuals with unresectable tumors or that prevent relapse after surgery. Several approaches to synergize ICB with pharmacological strategies targeting immunosuppressive fibroblasts, myeloid cells or regulatory T cells or cancer vaccines (for example, GVAX) genetically engineered to release immunostimulatory cytokines have been

✉ e-mail: [massimiliano.mazzone@kuleuven.vib.be](mailto:massimiliano.mazzone@kuleuven.vib.be)

proposed in mouse models or have been tested in the clinic<sup>10–14</sup>. In this context, tumor metabolism can compromise the function and fate of tumor-infiltrating immune cells and favor immunological tolerance<sup>15</sup>.

Cytidine deaminase (CDA) is an evolutionarily conserved enzyme of the pyrimidine salvage pathway responsible for the hydrolytic deamination of free cytidine and deoxycytidine to uridine and deoxyuridine, respectively. In some cancer cell lines, CDA protects newly synthesized DNA from incorporating epigenetically modified forms of cytidine<sup>16</sup>. Although CDA deaminates and inactivates cytidine analogs used as chemotherapeutic agents in cancer treatment (that is, gemcitabine, cytosine arabinoside and 5-azacytidine), thus playing a role in chemoresistance<sup>17–19</sup>, the possible contribution of CDA to the extracellular nucleotide pool and immunotherapy resistance has never been studied.

## Results

### CDA in cancer cells is associated with ICB resistance

To identify metabolic genes involved in immunotherapy resistance, we performed a meta-analysis on in-house-generated mouse bulk RNA-sequencing (RNA-seq) datasets and three publicly available pre-treatment transcriptomic datasets of tumors responsive and resistant to ICB, such as anti-CTLA-4 and anti-PD-1 (refs. 3,5,20; Extended Data Fig. 1a). Specifically, we first performed differential analysis between responsive and nonresponsive tumors on each dataset separately. We then ranked the genes by fold change and combined the rank numbers by calculating their rank product (Extended Data Fig. 1b). Finally, we filtered the ranked list for metabolic genes and calculated statistics by combining one-tailed *P* values across studies using Fisher's method<sup>20</sup>. From the top ten ranked candidates, we focused on *CDA* because nothing is known on pyrimidine metabolism in cancer immunotherapy (Fig. 1a and Extended Data Fig. 1b).

Of all the tumor types included in the meta-analysis, we focused on PDAC for the medical needs related to this aggressive and refractory tumor. Using the Xena PanCAN-GTex platform (and selecting for The Cancer Genome Atlas (TCGA) bulk RNA-seq datasets only), *CDA* expression was strongly upregulated in pancreatic tumor versus normal tissue (Fig. 1b). This finding was corroborated by immunohistochemistry for *CDA* in an independent cohort of 63 human treatment-naïve PDAC samples (referred to as cohort 1, stage I–III; N<sub>0</sub>–N<sub>2</sub>; Supplementary Table 1), revealing variable but selective expression of *CDA* in cancer cells but not in adjacent nontumor tissue (Fig. 1c). Furthermore, *CDA* expression was also significantly upregulated in colon, gastric and esophageal cancers compared to in their normal counterparts (Extended Data Fig. 2a).

Closer examination of the tumor microenvironment (TME) using a human PDAC publicly available single-cell RNA-seq (scRNA-seq) dataset<sup>21</sup> revealed *CDA* expression mainly in cancer cells and endothelial cells (ECs) with low expression in macrophages. The normal pancreatic epithelium (both acinar and ductal cells), fibroblasts and other immune cells, such as T, B and natural killer (NK) cells, showed no detectable *CDA* expression (Fig. 1d). However, data validation by coimmunostainings of nine PDAC sections randomly selected from the previous cohort 1 confirmed the histopathological observation that, at the protein level, *CDA* was expressed in neoplastic ducts, but not in macrophages or ECs (Fig. 1e,f).

Together, *CDA* induction in cancer cells and its correlation with ICB resistance suggest its possible role in hampering antitumor responses and immunotherapy efficacy.

### CDA in individuals with PDAC correlates with immunosuppression

By preselecting PDAC tumors from the TCGA PDAC cohort according to their highly immunosuppressive/low immunogenic landscape profile (that is, PDAC tumors showing high enrichment of a macrophage signature but decreased expression of a CD8<sup>+</sup> T cell signature), we observed that *CDA* expression was higher in this group than in the less

immunosuppressive groups (that is, low enrichment of a macrophage signature but higher expression of a CD8<sup>+</sup> T cell signature; Fig. 1g).

To validate these findings, we selected two homogeneous subsets of individuals with PDAC out of the above-mentioned cohort 1. In the first subset, we included 32 individuals with early-stage PDAC (stage I–IIa; N<sub>0</sub>), whereas in the second subset, we included 31 individuals with late-stage PDAC (stage IIb–III; N<sub>1</sub>–N<sub>2</sub>). To reduce the effect of intratumoral variability, the pathologist used macroblocks with cross-sections of the whole surgical specimen to evaluate areas of interest and identify margin and center areas. Individuals were dichotomized into CDA<sup>low</sup> and CDA<sup>high</sup> cancers (Supplementary Table 1). We found a significant correlation between *CDA* expression (set 1: CDA<sup>low</sup> *n* = 14, CDA<sup>high</sup> *n* = 18; set 2: CDA<sup>low</sup> *n* = 17, CDA<sup>high</sup> *n* = 14) in malignant ductal cells with intratumoral CD68<sup>+</sup> tumor-associated macrophage (TAM) infiltration or the CD206<sup>+</sup> immunosuppressive fraction, both at the tumor border and center (Fig. 1h and Extended Data Fig. 2b,c). Accordingly, CD8<sup>+</sup> T cell infiltration in the tumor center was significantly lower in CDA<sup>high</sup> PDAC, but it did not change at the tumor rim (Fig. 1h,i and Extended Data Fig. 2d). Vice versa, low *CDA* expression matched with reduced total and CD206<sup>+</sup> TAMs but with increased CD8<sup>+</sup> T cell infiltration (Fig. 1h,i and Extended Data Fig. 2b–d).

Moreover, the analysis of pretreatment bulk RNA-seq data from an independent set of seven PDAC tumors<sup>22</sup> revealed an association between high *CDA* expression and resistance to ICB (in combination with radiotherapy). Conversely, low *CDA* expression was associated with (partial) response (Fig. 1j).

Together, these data reinforce the idea that *CDA* upregulation may play an important role in shaping the immunosuppressive landscape of human PDAC and other tumors, possibly mounting immunotherapy resistance.

### Targeting CDA in PDAC cancer cells promotes anti-PD-1 efficacy

To assess the possible link between *CDA* expression in cancer cells and ICB resistance in PDAC, we used two mouse PDAC tumor engraftment models: orthotopic KPC tumors and subcutaneous (s.c.) Panc02 tumors. The Panc02 model is not reflective of human disease because it does not carry *KRAS* activation (occurring in 90% of human PDAC) and it presents more mutations and antigens than in human PDAC, but it is still resistant to ICB<sup>23</sup>. Instead, KPC cells, isolated from *LSL-Kras*<sup>G12D/+</sup>; *LSL-Trp53*<sup>R172H/+</sup>; *Pdx1:cre*<sup>Tg/+</sup> mice, carry the most frequent oncogenic features of human PDAC, namely *KRAS* activation and mutant p53 with loss of the wild-type function<sup>24</sup>.

First, we examined *Cda* expression in sorted cells from these two tumor models. In-house quantitative PCR with reverse transcription (RT–qPCR) data showed *Cda* expression in cancer cells and ECs, but not in macrophages or T cells (Extended Data Fig. 2e,f). In contrast to humans, some *Cda* expression was found in cancer-associated fibroblasts (Extended Data Fig. 2e,f). Publicly available scRNA-seq data from autochthonous tumors in genetically engineered KPC mice<sup>11</sup> showed the same pattern as observed in KPC tumor allografts (Extended Data Fig. 2g). Taken together, *CDA* is enriched in the cancer epithelial compartment in both humans and mice.

At this point, we genetically targeted *Cda* in mouse pancreatic cancer cell lines via CRISPR–Cas9. *Cda* targeting in Panc02 cells was achieved by testing two different single guide RNAs (sgCda1 or sgCda2, the latter referred to as sgCda) and a nontargeting sgRNA (sgNT) as a control (Extended Data Fig. 3a,b). KPC cells (that is, FC1245 and FC1199) were engineered with one of the two guide RNAs only (namely, sgCda; Extended Data Fig. 3f,g,i,j). *CDA* targeting did not alter *in vitro* proliferation (Extended Data Fig. 3s).

Subsequently, sgCda or sgNT Panc02 cells were injected s.c., while KPC FC1245 and FC1199 cells were inoculated orthotopically in C57BL/6 mice and treated with IgG or anti-PD-1. *CDA* targeting in Panc02 cancer cells resulted in decreased tumor growth and weight and complete

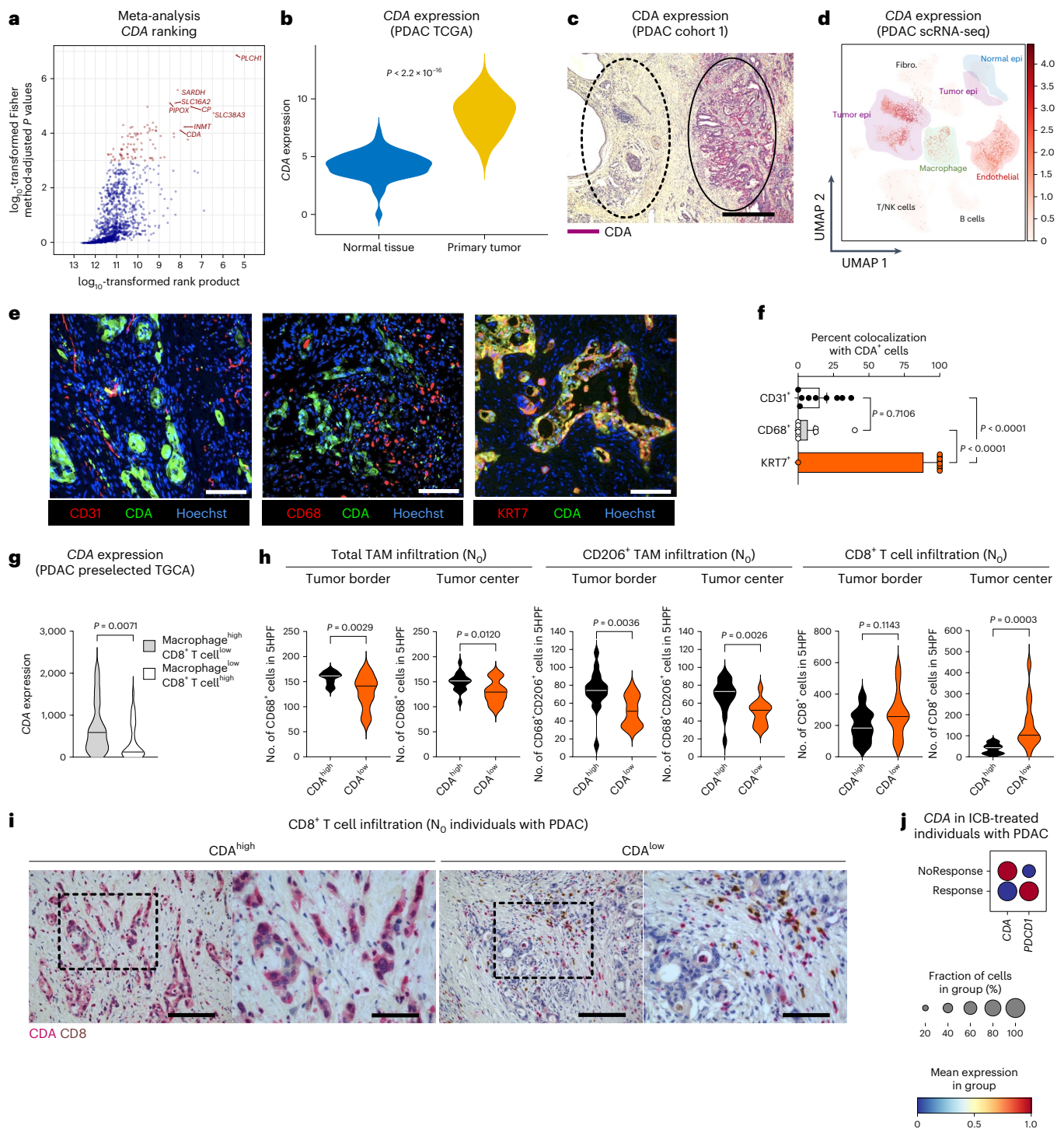


**Fig. 1 | CDA is associated with resistance to immunotherapy.** **a**, Meta-analysis on four datasets. Red indicates genes with adjusted  $P$  values of  $< 1 \times 10^{-3}$ ; CDA: 9 of 1,321; adjusted  $P$  value of  $< 1 \times 10^{-4}$ . **b**, CDA expression in pancreatic cancer ( $n = 183$ ) and normal pancreatic tissues ( $n = 167$ ). **c**, Representative image of CDA staining (purple) in tumor (right ellipse) and adjacent tissue (left ellipse) of an individual with PDAC (cohort 1,  $n = 63$ ); scale bar, 100  $\mu\text{m}$ . **d**, UMAP representing CDA expression in different cell populations of pancreatic tissue from treatment-naive individuals with PDAC ( $n = 24$ ). The number of cells analyzed is 83,960; epi, epithelial cells; Fibro., fibroblasts. **e, f**, Representative micrographs (**e**) and related quantification (percentage of colocalization; **f**) of CDA (green) with cancer cells;  $n = 9$  out of cohort 1; scale bar, 50  $\mu\text{m}$ . **g**, Violin plot of CDA expression in macrophage<sup>high</sup>CD8<sup>+</sup>T cell<sup>low</sup> ( $n = 64$ ) versus macrophage<sup>low</sup>CD8<sup>+</sup>T cell<sup>high</sup> ( $n = 31$ ) individuals with PDAC in TCGA. **h**, Histological analysis of treatment-naive, resectable PDAC tumors (out of cohort 1; stage I–IIa;  $N_0$ ). Violin

plots showing quantification of total CD68<sup>+</sup> (left), immunosuppressive CD206<sup>+</sup> TAMs (middle) and cytotoxic T cells (CD8<sup>+</sup>; right) at the tumor border or center (CDA<sup>high</sup>  $n = 18$  individuals with PDAC; CDA<sup>low</sup>  $n = 14$  individuals with PDAC); 5HPF, five high-power fields. **i**, Representative images of cytotoxic T cell (CD8; brown) infiltration in the tumor core (low magnification on the left and a zoom on the right) of an individual with PDAC (cohort 1,  $n = 63$ ); scale bars, 10  $\mu\text{m}$  (left) and 5  $\mu\text{m}$  (right). **j**, Dot plot of CDA and PDCDI expression in PDAC tumors from individuals before three cycles of ICB (combined with radiation on the second cycle). Mean expression is shown as color and is standard scaled (binarized), whereas dot size represents the fraction of samples with expression (Response  $n = 2$ ; NoResponse  $n = 5$ ). In **b–d** and **f–j**,  $n$  represents the number of individuals. Data were analyzed by unpaired, two-tailed Student's  $t$ -tests (**b**, **g** and **h**), one-way analysis of variance (ANOVA) with Tukey's multiple comparison test (**f**) and Fisher's combined probability test (one sided; **a**). Data are shown as mean  $\pm$  s.e.m.

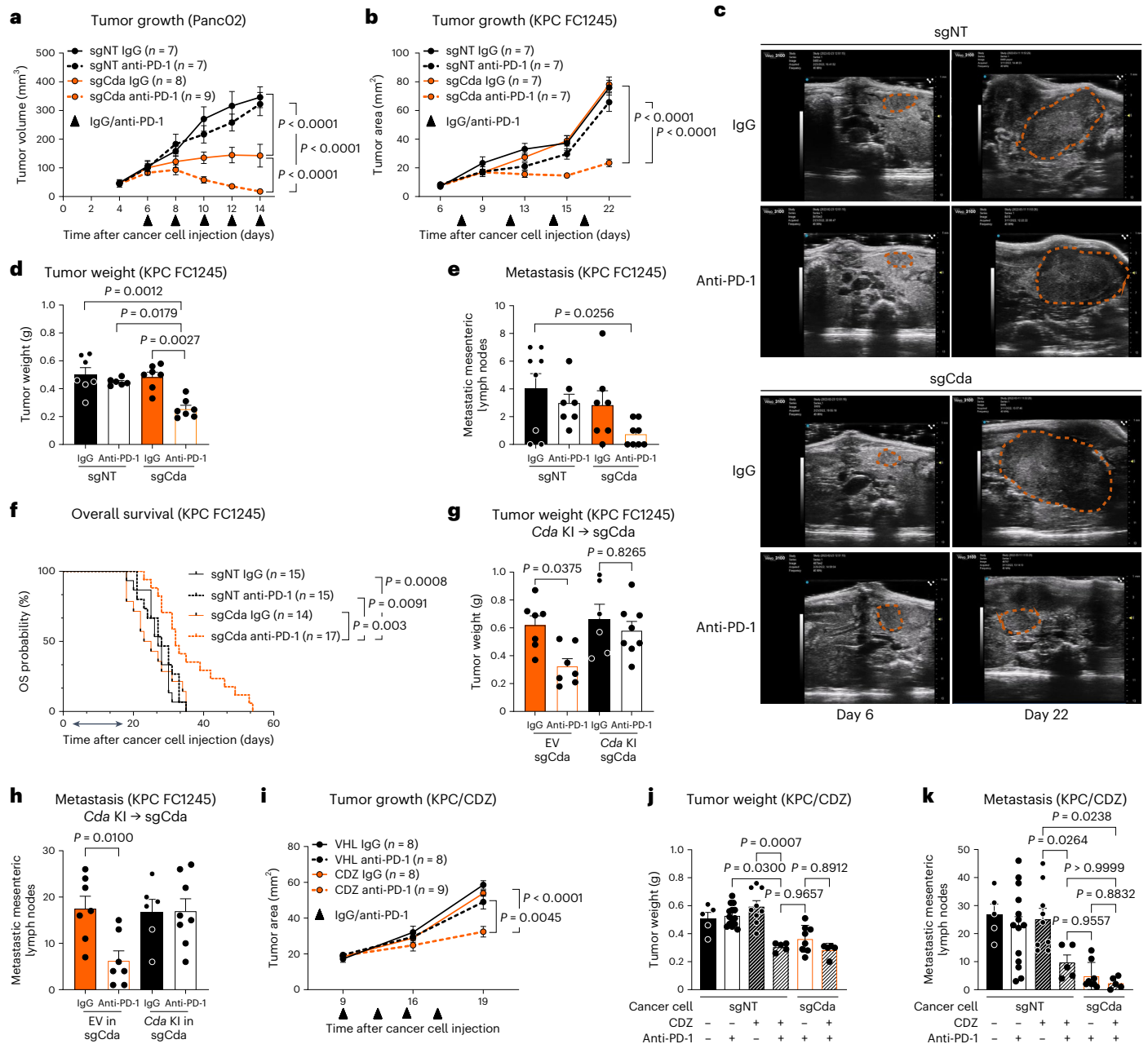


**Fig. 2 | Targeting CDA improves anti-PD-1 therapy efficacy. a**, Growth of sgNT (control) and sgCda s.c. Panc02 tumors treated with anti-PD-1 or control IgG (sgNT (IgG)  $n = 7$ , sgNT (anti-PD-1)  $n = 7$ , sgCda (IgG)  $n = 8$ , sgCda (anti-PD-1)  $n = 9$ ). The treatment regimen is indicated by the black arrowheads. **b**, Ultrasound-guided longitudinal measurements of sgNT and sgCda orthotopic KPC FC1245 tumors treated with anti-PD-1 or control IgG (sgNT (IgG)  $n = 7$ , sgNT (anti-PD-1)  $n = 7$ , sgCda (IgG)  $n = 7$ , sgCda (anti-PD-1)  $n = 7$ ). **c**, Representative images (ultrasound) at day 6 and day 22 after cancer cell injection of sgNT and sgCda KPC FC1245 tumors. **d**, Weight of KPC FC1245 sgNT and sgCda tumors at end stage treated with anti-PD-1 or control IgG (sgNT (IgG)  $n = 7$ , sgNT (anti-PD-1)  $n = 6$ , sgCda (IgG)  $n = 7$ , sgCda (anti-PD-1)  $n = 7$ ). **e**, Quantification of metastatic mesenteric lymph nodes in sgNT and sgCda KPC FC1245 tumor-bearing mice treated with anti-PD-1 or control IgG (sgNT (IgG)  $n = 8$ , sgNT (anti-PD-1)  $n = 7$ , sgCda (IgG)  $n = 7$ , sgCda (anti-PD-1)  $n = 8$ ). Treatment regimen is indicated in **b** by the black arrowheads. **f**, Kaplan–Meier curves of mice bearing tumors derived from sgNT and sgCda KPC FC1245 clones treated with anti-PD-1 or control IgG (sgNT (IgG)  $n = 15$ , sgNT (anti-PD-1)  $n = 15$ , sgCda clones (IgG)  $n = 14$ , sgCda clones (anti-PD-1)  $n = 17$ ). Data are representative of a pool of three independent experiments; OS, overall survival. **g**, Weight of control (EV in sgCda) and *Cda*

knock-in (*Cda* KI in sgCda) tumors treated with anti-PD-1 or control IgG. **h**, Quantification of metastatic mesenteric lymph nodes in control and *Cda* knock-in tumor-bearing mice treated with anti-PD-1 or control IgG (in **g–h**, EV (IgG)  $n = 7$ , EV (anti-PD-1)  $n = 7$ , *Cda* KI (IgG)  $n = 6$ , *Cda* KI (anti-PD-1)  $n = 8$ ). Data are representative of a pool of two independent experiments. **i**, Ultrasound-guided longitudinal measurements of orthotopic KPC FC1245 tumors treated with CDZ or vehicle (VHL) and anti-PD-1 or control IgG (vehicle (IgG)  $n = 8$ , VHL (anti-PD-1)  $n = 8$ , CDZ (IgG)  $n = 8$ , CDZ (anti-PD-1)  $n = 9$ ). Treatment regimen is indicated by the black arrowheads. **j**, Weight of sgNT and sgCda KPC FC1245 tumors treated with CDZ or vehicle and anti-PD-1 or IgG. **k**, Quantification of metastatic mesenteric lymph nodes in CDZ- or vehicle-treated sgNT and sgCda KPC FC1245 tumor-bearing mice in combination with anti-PD-1 or IgG (in **j–k**, vehicle sgNT (IgG)  $n = 5$ , vehicle sgNT (anti-PD-1)  $n = 14$ , CDZ sgNT (IgG)  $n = 9$ , CDZ sgNT (anti-PD-1)  $n = 5$ , vehicle sgCda (IgG)  $n = 8$ , CDZ sgCda (anti-PD-1)  $n = 5$ ). In **a**, **b** and **d–k**,  $n$  represents biological replicates. Data were analyzed by two-way repeated measures ANOVA (**a**, **b** and **i**), two-way ANOVA with Tukey's multiple comparison test (**d**, **e**, **g**, **h**, **j** and **k**) or log-rank hypothesis test (Mantel–Cox test; **f**). Data are shown as mean  $\pm$  s.e.m.

regression following anti-PD-1 treatment compared to resistant control (sgNT) tumors (Fig. 2a and Extended Data Fig. 3c–e). By contrast, longitudinal kinetics via ultrasound or end-stage analysis of orthotopically engrafted KPC FC1245 tumors showed that sgCda did not achieve any tumor growth inhibition (Fig. 2b–d and Extended Data Fig. 3h). However, although control (sgNT) tumors displayed no to very little response to anti-PD-1 treatment, mice engrafted with sgCda cancer cells displayed a tumor reduction of 40% to 70% compared to IgG-treated sgNT controls (Fig. 2b–d and Extended Data Fig. 3h). Furthermore, mesenteric lymph node metastases (evaluated macroscopically as in Mazzone et al.<sup>25</sup> and Casazza et al.<sup>26</sup>) were very few in the sgCda plus anti-PD-1 condition (Fig. 2e and Extended Data Fig. 3h). Consistently, genetic inhibition of *Cda* significantly improved the survival rate of KPC FC1245 tumor-bearing mice after anti-PD-1 treatment, whereas the three other conditions were unchanged (Fig. 2f), supporting the idea that CDA targeting overcomes anti-PD-1 resistance. Similar findings were observed by using the KPC FC1199 clone (Extended Data Fig. 3k,l). Of note, the *in vivo* levels of *Pdcd1* (encoding PD-1) or *Cd274* (encoding the PD-1 ligand PD-L1), both *in vivo* and in cultured cancer cells, were not altered by CDA depletion (Extended Data Fig. 3m–o).

We then reintroduced a cDNA encoding CDA in sgCda KPC FC1245 cells and injected them orthotopically (Extended Data Fig. 3p). Re-expression of CDA re-established anti-PD-1 resistance, as suggested by the increase in tumor weight and mesenteric lymph node metastases to the levels observed in IgG-treated groups (Fig. 2g,h). This experiment excludes off-target effects and proves that tumor regression is not linked to neoantigen formation. Mutational burden in sgNT and sgCda cancer cells corroborated this conclusion (Extended Data Fig. 3q).

To determine whether pharmacological blockade of CDA could be exploited therapeutically, we used the well-known CDA inhibitor cedazuridine (CDZ), which is clinically used in combination with decitabine in myeloid malignancies<sup>27,28</sup>. When administered orally to KPC FC1245 tumor-bearing mice in combination with IgG or anti-PD-1, CDZ did not cause overt toxicity (Extended Data Fig. 3r). Combined CDZ and anti-PD-1 therapy decreased tumor growth (as assessed longitudinally by ultrasound), end-stage tumor weight and mesenteric lymph node metastases (Fig. 2i–k). We did not observe any additional effect of CDZ when treating sgCda tumors, suggesting that the phenotype is due to CDA inhibition in cancer cells only (Fig. 2j,k).

Thus, both genetic and pharmacological CDA inhibition in PDAC models overcome immunotherapy resistance.

### Targeting CDA in PDAC cancer cells alters the TME

Histological analysis revealed that in control (sgNT) s.c. Panc02 tumors, cytotoxic CD8<sup>+</sup> T cells grouped at the tumor border, whereas CD8<sup>+</sup> T cells were missing in the tumor center, disclosing the inability of CD8<sup>+</sup> T cells to invade the tumor. However, intratumoral CD8<sup>+</sup> T cell infiltration was significantly increased in CDA-targeted tumors (Fig. 3a,b). Flow cytometry analysis confirmed the increased infiltration of total and activated CD8<sup>+</sup> T cells in IgG-treated sgCda Panc02 tumors (Fig. 3c). Conversely, both total and immunosuppressive CD206<sup>+</sup> macrophages were diminished in sgCda Panc02 tumors (Fig. 3d,e and Extended Data Fig. 4a). No changes were observed in CD4<sup>+</sup> or regulatory T cells, neutrophils, NK cells or dendritic cells (DCs; Extended Data Fig. 4b,c). The effect of combined CDA targeting and anti-PD-1 could not be analyzed due to tumor regression.

In the orthotopic KPC model, CDA targeting alone (IgG group) did not alter the numbers of total or activated CD8<sup>+</sup> T cells (Fig. 3f), which were, however, higher after anti-PD-1 treatment than in anti-PD-1-treated sgNT tumors. CD4<sup>+</sup> T cells were, in general, unaffected (Fig. 3f). By contrast, total and CD206<sup>+</sup> TAM infiltration was reduced by CDA depletion, and anti-PD-1 treatment did not change this effect (Fig. 3g).

Thus, CDA inhibition in cancer cells breaks immunosuppression and enables T cell response to anti-PD-1.

### CDA contribution to anti-PD-1 resistance in other tumor types

We then extended our findings to other tumor types included in the initial meta-analysis. We chose the orthotopic YUMM1.7 melanoma cell line because it is anti-PD-1 resistant and presents genetic alterations seen in a large subset of human melanomas (*Braf*<sup>V600E/+</sup>; *Pten*<sup>-/-</sup>; *Cdkn2*<sup>-/-</sup>)<sup>29</sup>. CDA depletion in combination with anti-PD-1 treatment reduced tumor growth (Fig. 4a and Extended Data Fig. 4d,e). Moreover, CDA targeting was sufficient to reduce both total and CD206<sup>+</sup> TAM infiltration (Fig. 4b), whereas its combination with anti-PD-1 treatment only enhanced CD8<sup>+</sup> T cell activation (Fig. 4c). *In vitro* proliferation of sgNT and sgCda YUMM1.7 cells did not differ (Extended Data Fig. 4f).

We also assessed whether CDA overexpression could establish ICB resistance. We picked the anti-PD-1-responsive colorectal cancer model (MC38) included in our meta-analysis that expresses low levels of *Cda* (Extended Data Fig. 4g). *Cda* overexpression in MC38 cells (Extended Data Fig. 4h,i) rendered the tumor more aggressive and resistant to anti-PD-1 therapy (Fig. 4d,e) as a result of impaired induction of a T cell response following anti-PD-1 administration. Although empty vector (EV) control MC38 tumors showed increased levels of total and early activated (CD69<sup>+</sup>) CD8<sup>+</sup> T cells following anti-PD-1 treatment, CDA overexpression completely abrogated this CD8<sup>+</sup> T cell response to anti-PD-1 therapy (Fig. 4f).

Overall, CDA induction in cancer cells mediates anti-PD-1 resistance in different tumor types, such as PDAC, melanoma and colorectal cancer.

### CDA targeting engages the immune system against the tumor

Based on the modified immune landscape after tweaking CDA expression in cancer cells and comparable tumor growth of sgNT and sgCda Panc02 cancer cells in immunodeficient (nude) mice (Extended Data Fig. 4j,k), we tested the contribution of CD8<sup>+</sup> T cells and macrophages after CDA targeting. To this end, we performed CD8<sup>+</sup> T cell depletion and macrophage adoptive transfer experiments, respectively.

First, we depleted CD8<sup>+</sup> T cells in sgNT and sgCda KPC FC1245 tumor-bearing mice all treated with anti-PD-1 therapy (Extended Data Fig. 4l). CD8<sup>+</sup> T cell depletion rescued the growth of sgCda tumors to the level of control (sgNT) tumors; in mice treated with depleting anti-CD8, sgNT tumors were slightly bigger than their counterparts in nondepleted mice (Fig. 4g).

When co-injected TAM-like macrophages (herein TAMs-L, which are bone marrow-derived macrophages (BMDMs) conditioned for 18 h with KPC FC1245 tumor-conditioned medium<sup>30</sup>) with sgNT or sgCda KPC FC1245 cells, as described previously<sup>31</sup>. Nine days after orthotopic injections, mice were treated with anti-PD-1. Adoptive transfer of TAMs-L in sgCda tumors was sufficient to abolish their growth defect, whereas no changes were observed after TAMs-L co-injection in sgNT tumors (Fig. 4h). Again, CDA depletion increased cytotoxic CD8<sup>+</sup> T cell infiltration at the core without affecting their abundance at the tumor rim. TAMs-L co-injection completely abrogated this effect, leading to a reduction of cytotoxic CD8<sup>+</sup> T cells in the tumor core (Fig. 4i). These data suggest that CDA-depleted cancer cells somehow lose their capacity to recruit macrophages and sustain their immunosuppressive phenotype.

Killing of ovalbumin (OVA)-expressing cancer cells by antigen-specific CD8<sup>+</sup> T (OT-I) cells, major histocompatibility complex class I (MHC class I) exposed to the cell membrane and antigen presentation in OVA-expressing cancer cells (both at baseline and after interferon- $\gamma$  (IFN $\gamma$ ) stimulation) were all not affected by *Cda* deletion (Extended Data Fig. 4m–o). However, in the presence of BMDMs and OVA<sup>+</sup> sgCda cancer cells, OT-I T cells were activated more efficiently than when added to cocultures of BMDMs and OVA<sup>+</sup> sgNT cancer cells. By contrast, coculture of sgNT or sgCda cancer cells only with OT-I T cells did not change their activation (Fig. 4j).

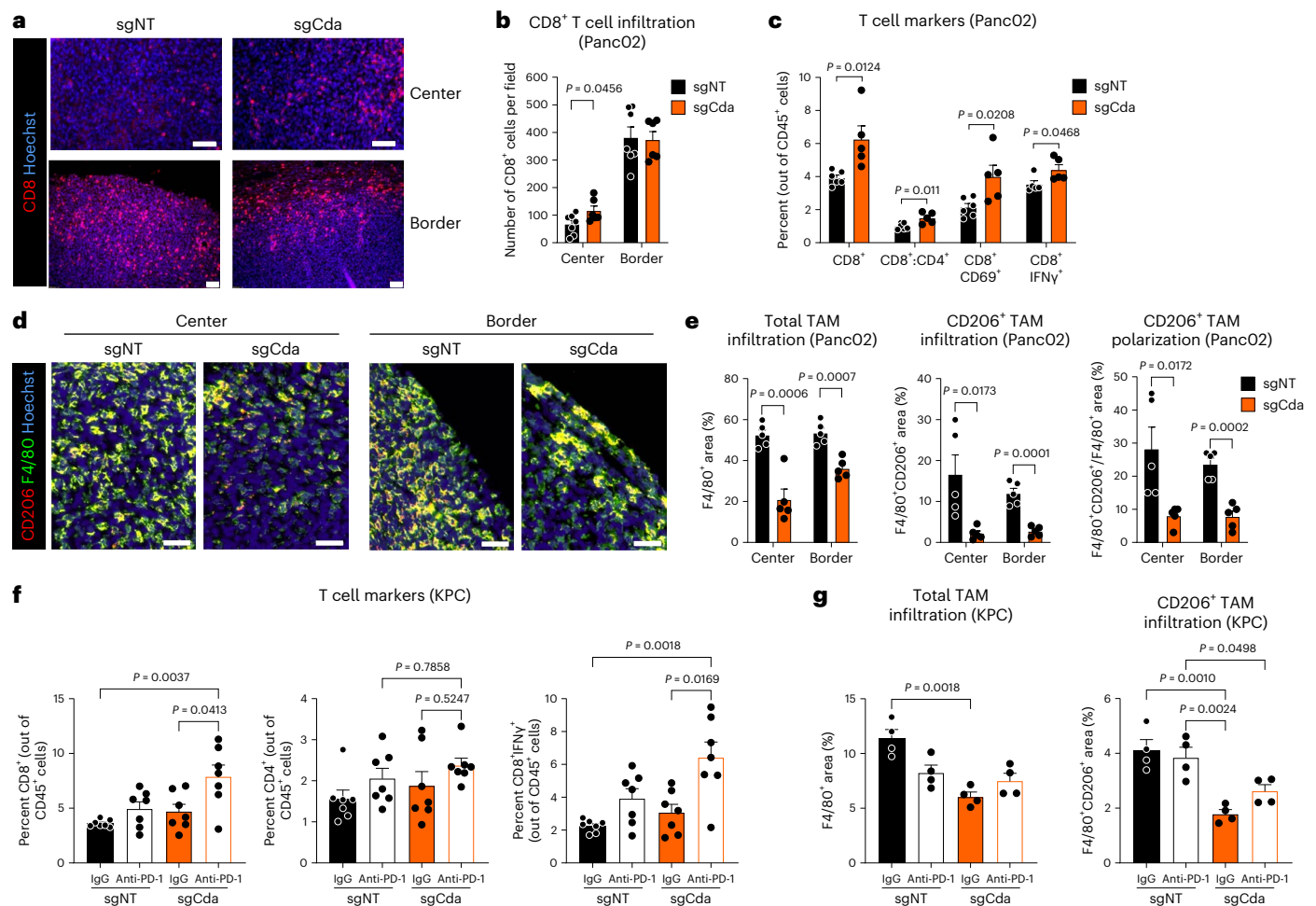


**Fig. 3 | Targeting CDA skews TAMs toward a T cell stimulatory phenotype.** **a–c**, T cell immune cell landscape in sgNT and sgCda (IgG-treated) s.c. Panc02 tumors. Representative micrographs of cytotoxic CD8<sup>+</sup> T cells of sgNT and sgCda Panc02 tumors (center, top; border, bottom; **a**) and related histological quantification are shown (**b**); sgNT (center)  $n = 7$ , sgNT (border)  $n = 7$ , sgCda (center)  $n = 6$ , sgCda (border)  $n = 6$ . **c**, Flow cytometric quantification of cytotoxic T cells (CD8<sup>+</sup>), CD8<sup>+</sup>:CD4<sup>+</sup> T cell ratio and activated cytotoxic T cells (CD8<sup>+</sup>CD69<sup>+</sup> and CD8<sup>+</sup>IFN $\gamma$ <sup>+</sup>) in sgNT and sgCda (IgG-treated) Panc02 tumors (CD8<sup>+</sup>IFN $\gamma$ <sup>+</sup>, sgNT  $n = 5$  and sgCda  $n = 5$ ; all others, sgNT  $n = 6$  and sgCda  $n = 5$ ); scale bars, 50  $\mu$ m (top) and 10  $\mu$ m (bottom). **d, e**, Macrophage immune landscape in sgNT and sgCda (IgG-treated) s.c. Panc02 tumors. Representative micrographs (**d**) and related histological quantification (**e**) of total TAM infiltration (left; percentage of F4/80<sup>+</sup> cells out of total area), CD206<sup>+</sup> TAM infiltration (middle; percentage of F4/80<sup>+</sup>CD206<sup>+</sup> cells out of total area) and CD206<sup>+</sup> TAM polarization (right; F4/80<sup>+</sup>CD206<sup>+</sup> cells out of F4/80<sup>+</sup> area) in sgNT and sgCda (IgG-treated) Panc02 tumors (center and border) are shown (sgNT (center)  $n = 5$ , sgNT (border)  $n = 5$ , sgCda (center)  $n = 5$ , sgCda (border)  $n = 5$ ); scale bar, 50  $\mu$ m. **f**, T cell immune cell landscape in sgNT and sgCda orthotopic KPC FC1245 tumors. Flow cytometric quantification of cytotoxic T cells (left; CD8<sup>+</sup>), helper T cells (middle; CD4<sup>+</sup>) and activated T cells (right; CD8<sup>+</sup>IFN $\gamma$ <sup>+</sup>) in sgNT and sgCda orthotopic KPC tumors treated with anti-PD-1 or control IgG (sgNT (IgG)  $n = 7$ , sgNT (anti-PD-1)  $n = 7$ , sgCda (IgG)  $n = 7$ , sgCda (anti-PD-1)  $n = 7$ ). **g**, Macrophage immune landscape in sgNT and sgCda orthotopic KPC FC1245 tumors. Histological quantification of total TAM infiltration (left; percentage of F4/80<sup>+</sup> cells out of total area) and CD206<sup>+</sup> TAM infiltration (right; percentage of F4/80<sup>+</sup>CD206<sup>+</sup> cells out of total area) in sgNT and sgCda orthotopic KPC tumors treated with anti-PD-1 or control IgG (sgNT (IgG)  $n = 4$ , sgNT (anti-PD-1)  $n = 4$ , sgCda (IgG)  $n = 4$ , sgCda (anti-PD-1)  $n = 4$ ). In **b** and **c** and **e–g**,  $n$  represents biological replicates. Data were analyzed by multiple unpaired, two-tailed Student's *t*-tests (**b**, **c** and **e**), two-way ANOVA with Tukey's multiple comparison test (**f** and **g**) or two-way repeated measures ANOVA (**h**). Data are shown as mean  $\pm$  s.e.m.

These data argue that CDA depletion in cancer cells sensitizes tumors to immunotherapy, possibly by defeating immunosuppressive TAMs and imposing their switch toward an immunostimulatory phenotype.

### CDA targeting limits the release of uracil nucleotides

By using a supraphysiological concentration of [<sup>13</sup>C,<sup>15</sup>N<sub>3</sub>]-labeled cytidine (that is, 100  $\mu$ M), we observed a decrease in intracellular uridine levels, which was mirrored by the accumulation of intracellular cytidine in sgCda versus sgNT cells (both KPC and Panc02; Fig. 5a,b and Extended Data Fig. 5a,b). In line with a reduced deamination of cytidine into uridine, intracellular abundance of [<sup>13</sup>C,<sup>15</sup>N<sub>3</sub>]cytidine remained higher in sgCda KPC cells than in CDA-proficient control cells (Fig. 5c), with a concomitant reduction of uridine production (Fig. 5d). Consistent with

the decrease in intracellular uridine, sgCda KPC FC1245 cells showed reduced intracellular levels of uracil nucleotides (UMP, UDP and UTP) compared to sgNT cells (Fig. 5e). The fraction of cytidine contributing to the uracil nucleotide pool is likely not reflecting physiology because here a supraphysiological cytidine concentration has been added to the culture medium. However, although the relative contribution of extracellular cytidine to the uracil nucleotide pool will depend on the concentration of cytidine used and the amount of extracellular uridine present, our labeling experiment highlights how CDA could take part in the generation of this pool. This difference in uracil nucleotides in sgCda versus sgNT KPC FC1245 cells did not affect DNA or RNA synthesis (Extended Data Fig. 5c). No major changes in adenine and cytosine nucleotides (that is, AMP, ADP and ATP and CMP, CDP and CTP, respectively) or in UDP-hexose (Extended Data Fig. 5d–f) were observed.

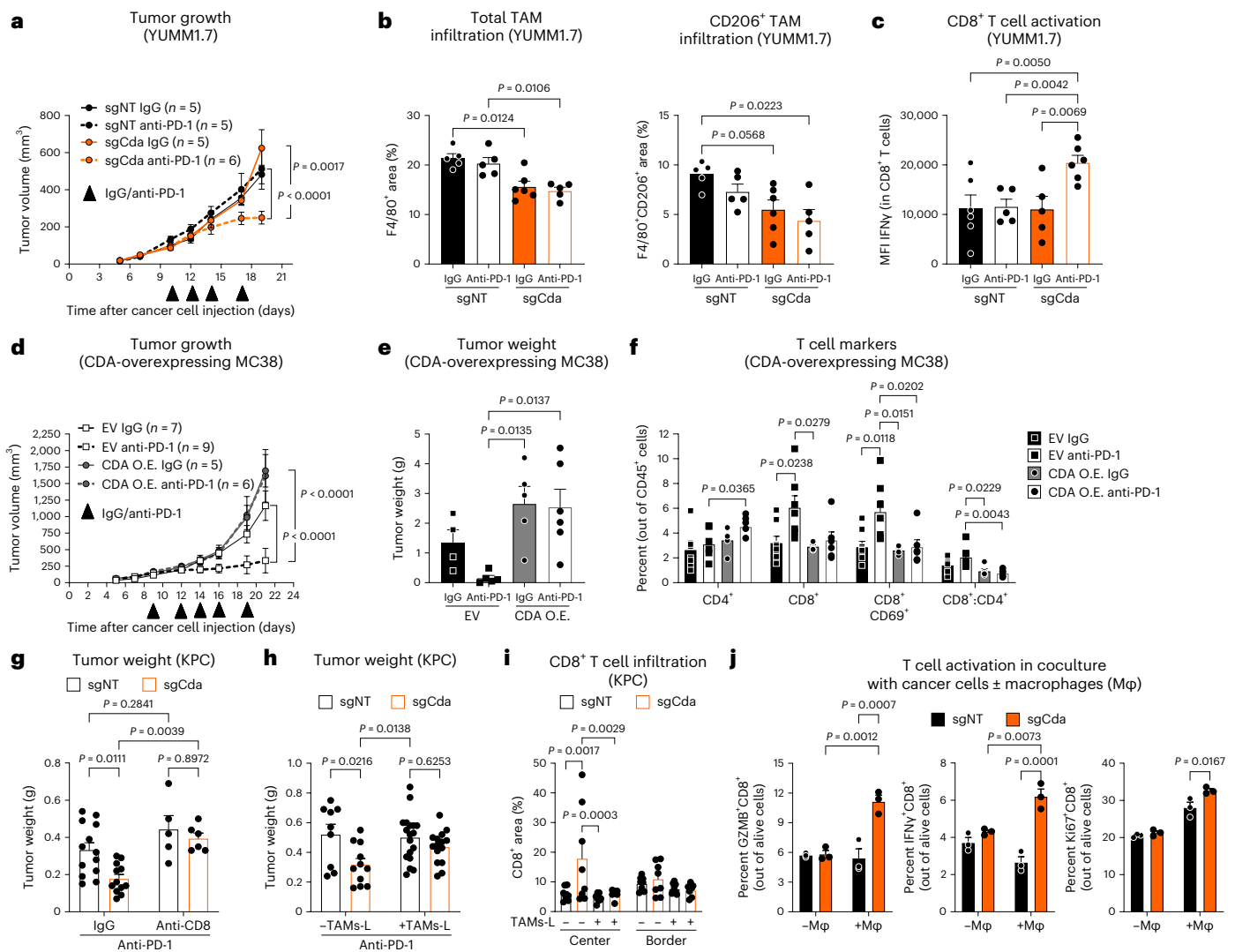


**Fig. 4 | Targeting CDA overcomes anti-PD-1 resistance by shaping the TME.**

**a–c**, Tumor volume (**a**), histological quantification of total TAM infiltration (percentage of F4/80<sup>+</sup> cells out of total area) and CD206<sup>+</sup> TAM infiltration (percentage of F4/80<sup>+</sup>CD206<sup>+</sup> cells out of total area; **b**) and flow cytometric quantification of activated cytotoxic CD8<sup>+</sup> T cells (mean fluorescence intensity (MFI) IFN $\gamma$ ) in sgNT and sgCda orthotopic YUMM1.7 tumors treated with anti-PD-1 or control IgG (**c**: sgNT (IgG)  $n = 5$ , sgNT (anti-PD-1)  $n = 5$ , sgCda (IgG)  $n = 5$ , sgCda (anti-PD-1)  $n = 6$  (**a**); sgNT (IgG)  $n = 5$ , sgNT (anti-PD-1)  $n = 5$ , sgCda (IgG)  $n = 6$ , sgCda (anti-PD-1)  $n = 5$  (**b**); sgNT (IgG)  $n = 6$ , sgNT (anti-PD-1)  $n = 5$ , sgCda (IgG)  $n = 5$ , sgCda (anti-PD-1)  $n = 6$  (**c**)). Treatment regimen is indicated in **a** by the black arrowheads. **d, e**, Volume (**d**) and weight of MC38 tumors over-expressing CDA (CDA O.E.) or their control (EV) treated with anti-PD-1 or control IgG (**e**). **f**, Flow cytometric quantification of intratumoral helper T cells (CD4<sup>+</sup>), cytotoxic T cells (CD8<sup>+</sup>), early activated T cells (CD8<sup>+</sup>CD69<sup>+</sup>) and CD8<sup>+</sup>:CD4<sup>+</sup> T cell ratio (IgG  $n = 5$ , CDA O.E. (anti-PD-1)  $n = 6$ , EV (IgG)  $n = 4–7$ , EV (anti-PD-1)  $n = 5–9$ ). Treatment regimen is indicated in **d** by the black arrowheads. **g**, Weight of sgNT and sgCda orthotopic KPC FC1245 tumors in mice treated with

IgG or CD8-depleting antibody. All mice were treated with anti-PD-1 (sgNT (IgG)  $n = 13$ , sgNT (anti-CD8)  $n = 5$ , sgCda (IgG)  $n = 12$ , sgCda (anti-CD8)  $n = 6$ ). Data are representative of a pool of two independent experiments. **h**, Weight of sgNT and sgCda orthotopic KPC FC1245 tumors resulting from cancer cells implanted alone or with TAMs-L (sgNT (-TAMs-L)  $n = 9$ , sgNT (+TAMs-L)  $n = 18$ , sgCda (-TAMs-L)  $n = 11$ , sgCda (+TAMs-L)  $n = 15$ ). Data are representative of a pool of two independent experiments. **i**, Histological quantification of cytotoxic CD8<sup>+</sup> T cells (center and border; sgNT (-TAMs-L)  $n = 8$ , sgNT (+TAMs-L)  $n = 9$ , sgCda (-TAMs-L)  $n = 8$ , sgCda (+TAMs-L)  $n = 7$ ). All mice were treated with anti-PD-1. **j**, Flow cytometric quantification of activated (GZMB<sup>+</sup> and IFN $\gamma$ <sup>+</sup>) and proliferating (Ki67<sup>+</sup>) OT-I CD8<sup>+</sup> T cells in coculture with OVA-expressing sgNT or sgCda Panc02 cells with or without BMDMs (M $\phi$ ;  $n = 3$ ). In **a–i**,  $n$  represents biological replicates, whereas in **j**,  $n$  represents independently collected cell seedings. Data were analyzed by two-way ANOVA with Tukey's multiple comparison test (**b, c, g, h** and **j**), two-way repeated measures ANOVA (**a** and **d**), one-way ANOVA with Tukey's multiple comparison test (**e** and **f**) or two-way ANOVA with a Sidak's multiple comparison test (**i**). Data are shown as mean  $\pm$  s.e.m.

Also, no changes were observed in [<sup>13</sup>C,<sup>15</sup>N<sub>2</sub>]glutamine contribution to uracil-containing nucleotides after CDA depletion, suggesting that the de novo pyrimidine nucleotide synthesis rate was not affected (Extended Data Fig. 5g). We also confirmed a reduction in intracellular uracil nucleotide levels in sgCda Panc02 cells, without any differences in adenine and cytosine nucleotides or in UDP-hexose (Extended Data Fig. 5h–j). In general, cytidine (that is, the substrate of CDA) was found in mouse serum (that is,  $\sim 1$   $\mu$ M; Extended Data Fig. 5k) and in the tumor interstitial fluid (TIF; that is,  $\sim 10$   $\mu$ M; Fig. 5f; as previously reported<sup>32</sup>)

and also in vitro in absolute fetal bovine serum (FBS) and in the culture medium of both macrophages and dying KPC FC1245 cells (Extended Data Fig. 5k). Liquid chromatography–mass spectrometry (LC–MS) analysis of TIFs showed that more cytidine and less uridine was found in sgCda tumors than in sgNT tumors (Fig. 5f). Glucose and glutamine levels were the same (Extended Data Fig. 5l).

Because uracil nucleotides are important signaling molecules that activate G-protein-coupled membrane receptors of the P2Y family<sup>33</sup>, we hypothesized that the release of UTP and UDP by cancer cells is a

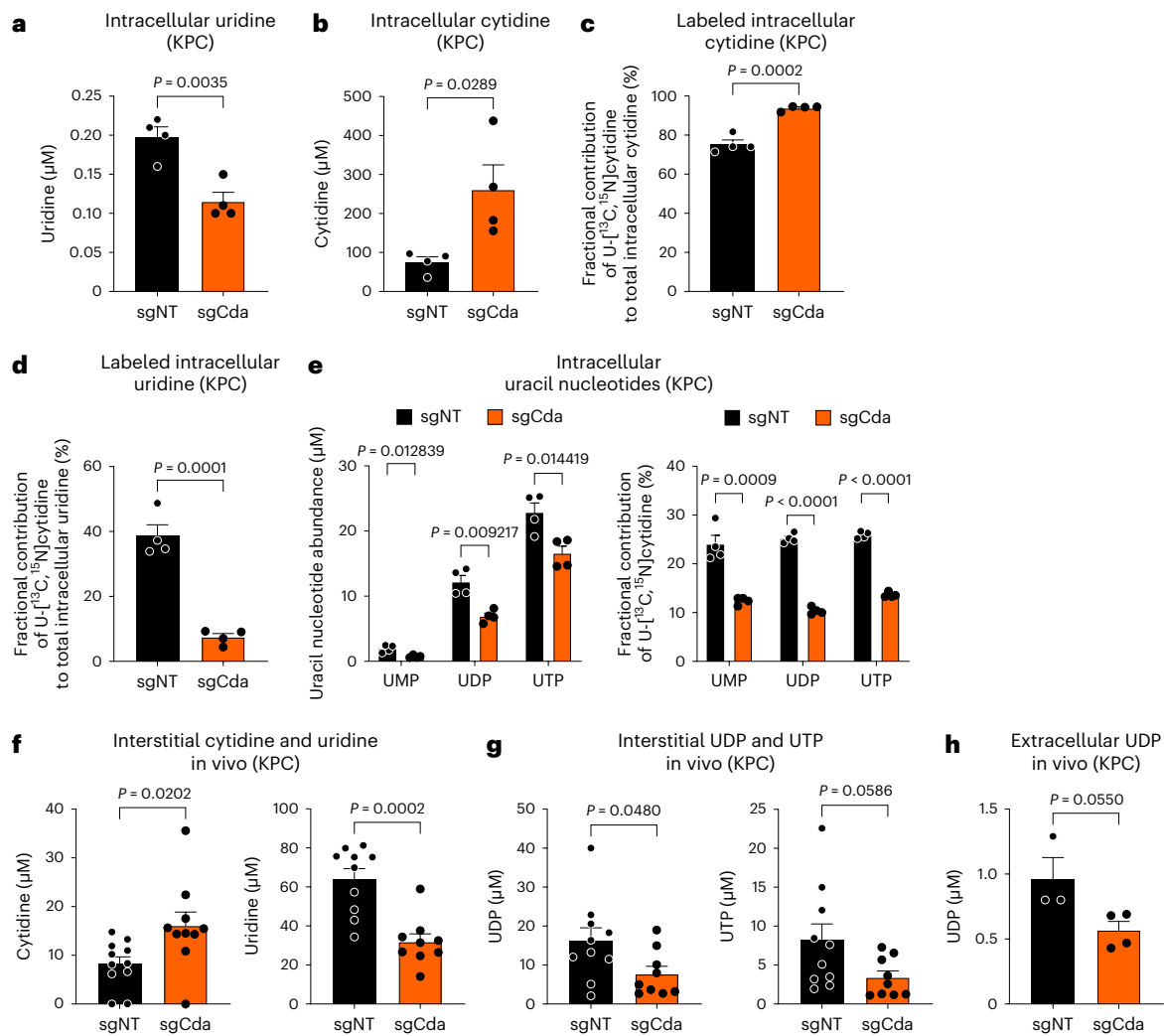


**Fig. 5 | CDA regulates uracil nucleotide production by cancer cells.**

**a, b**, Intracellular abundance of total uridine (**a**) and cytidine (**b**) in sgNT and sgCda KPC FC1245 cells (sgNT  $n = 4$  and sgCda  $n = 4$ ). **c, d**, Fractional contribution (percentage of labeled metabolite out of total amount) of supplemented 0.1 mM [ $^{13}\text{C}_9, ^{15}\text{N}_3$ ]cytidine to the intracellular cytidine (**c**) and uridine (**d**) pools in sgNT and sgCda KPC FC1245 cells (sgNT  $n = 4$  and sgCda  $n = 4$ ). **e**, Left, intracellular levels of uracil nucleotides (UMP, UDP and UTP) in sgNT and sgCda KPC FC1245 cells. Right, fractional contribution of supplemented 0.1 mM [ $^{13}\text{C}_9, ^{15}\text{N}_3$ ]cytidine to the intracellular uracil nucleotide pools (sgNT  $n = 4$  and sgCda  $n = 4$ ). **f**, Extracellular levels of cytidine (left) and uridine (right) in the interstitial fluid of orthotopic sgNT and sgCda KPC FC1245 tumors (sgNT  $n = 11$  and sgCda  $n = 10$  (left); sgNT  $n = 10$  and sgCda  $n = 9$  (right)). **g**, Extracellular levels of UDP (left) and UTP (right) in the interstitial fluid of orthotopic sgNT and sgCda KPC FC1245

tumors (sgNT  $n = 10$  and sgCda  $n = 9$ ). **h**, Extracellular levels of UDP in the culture medium of sgNT and sgCda KPC FC1245 cells (sgNT  $n = 3$  and sgCda  $n = 4$ ). In **a–e** and **h**,  $n$  represents independently collected cell seedings. In **f** and **g**,  $n$  represents biological replicates. In **a–g**, cytidine, uridine and uracil-containing nucleotides were measured by using LC–MS. In **h**, UDP in the culture medium was measured by using enzyme-linked immunosorbent assays. In **a–e**, KPC FC1245 cells were cultured in DMEM supplemented with 10% dialyzed FBS (to remove the naturally present cytidine) and 0.1 mM [ $^{13}\text{C}_9, ^{15}\text{N}_3$ ]cytidine. In **h**, KPC FC1245 cells were cultured in DMEM supplemented with 10% dialyzed FBS (to remove the naturally present cytidine) and 0.1 mM unlabeled cytidine. Data were analyzed by unpaired, two-tailed Student's  $t$ -tests (**a–d** and **f–h**) or multiple unpaired, two-tailed Student's  $t$ -tests (**e**). Data are shown as mean  $\pm$  s.e.m.

determinant factor in CDA-dependent resistance to anti-PD-1 therapy. First, we measured UDP and UTP levels in the extracellular milieu of sgCda and sgNT KPC FC1245 tumors. CDA depletion resulted in reduced UDP (and UTP) in the TIF (Fig. 5g). By using a protocol to assess extracellular nucleotide release in response to stress conditions<sup>34</sup>, we found that UDP (but not ATP) was also decreased in the culture medium of sgCda versus sgNT cancer cells (Fig. 5h and Extended Data Fig. 5m).

These results suggest that, in cancer cells, CDA is engaged in a pathway leading to the synthesis and release of uracil nucleotides.

#### CDA-expressing cancer cells recruit $\text{P2Y}_6^+$ macrophages

$\text{P2Y}_2$ ,  $\text{P2Y}_4$ ,  $\text{P2Y}_6$  and  $\text{P2Y}_{14}$  of the  $\text{P2Y}$  receptor family are pyrimidine-selective receptors that can be activated by UDP, UTP or, in the case

of  $\text{P2Y}_{14}$ , UDP-glucose<sup>35–37</sup>. Analysis of publicly available human PDAC scRNA-seq data<sup>21</sup> revealed that  $\text{P2RY2}$  was weakly expressed in tumor epithelial cells and ECs,  $\text{P2RY4}$  was not detectable,  $\text{P2RY6}$  was strongly expressed in macrophages and ECs, and  $\text{P2RY14}$  expression was restricted to fibroblasts, T and B cells and a small subset of macrophages (Fig. 6a). Uniform manifold approximation and projection (UMAP) of different myeloid cell/macrophage subclusters showed that  $\text{P2RY6}$  expression is the most widespread among the different macrophage clusters and is completely absent in  $\text{MRC1}^+$  ( $\text{CD206}^+$ ) pro-inflammatory macrophages (cluster 3; Fig. 6b). Conversely,  $\text{P2RY14}$  expression was mainly detected in monocyte-derived DC1 (cluster 7) and DC3 (cluster 4) only (Fig. 6b). Dot plots of  $\text{P2RY2}$ ,  $\text{P2RY6}$  and  $\text{P2RY14}$  expression in subclustered myeloid cells/macrophages revealed the strongest expression for  $\text{P2RY6}$  (Fig. 6b). Comparable results were



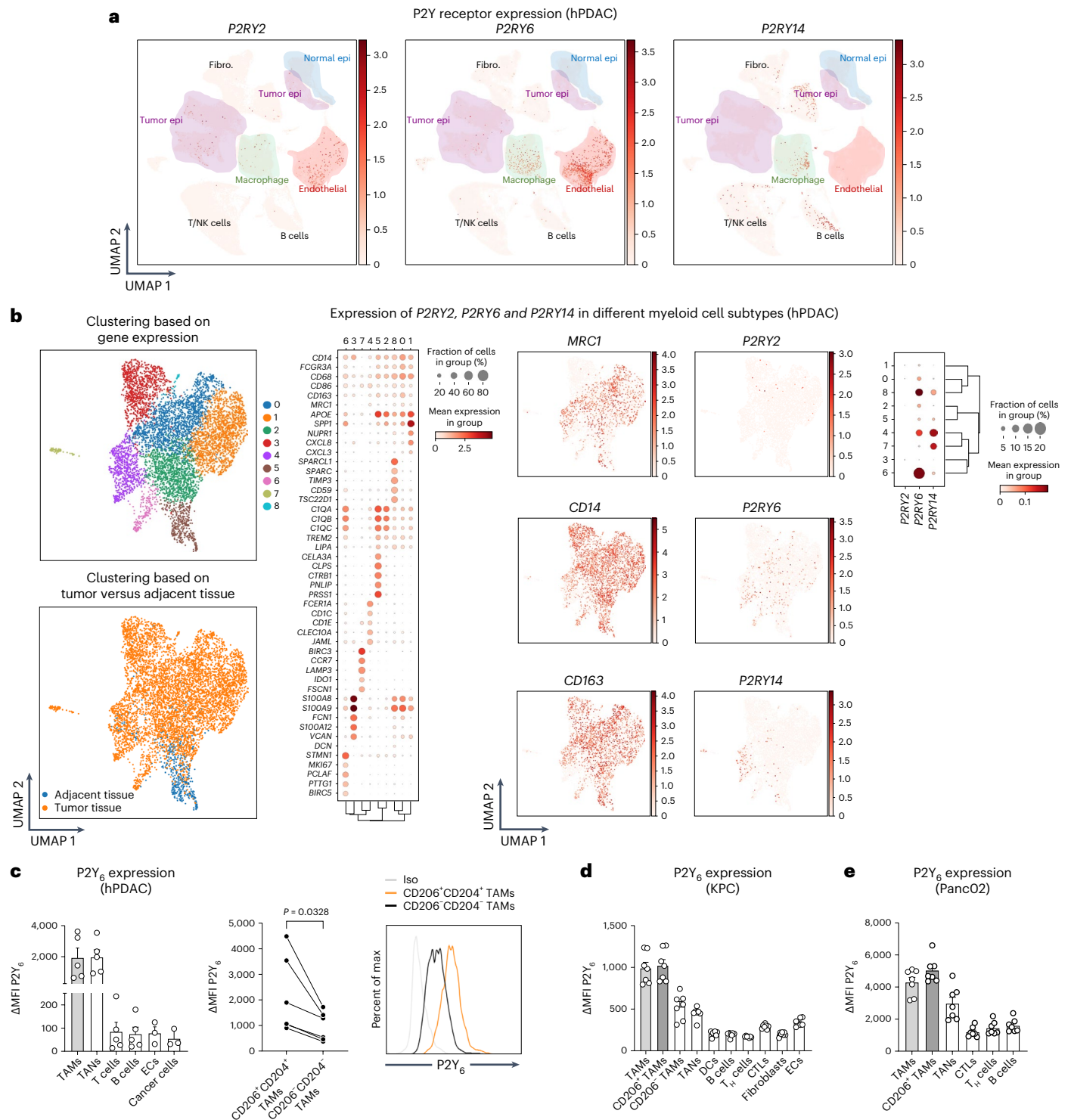


**Fig. 6 | Expression profile of the UDP cognate receptor *P2Y6*.** **a**, UMAP of *P2RY2*, *P2RY6* and *P2RY14* expression in different cell populations of pancreatic tissue from treatment-naive individuals with PDAC ( $n = 24$ ). The number of cells analyzed is 83,960. **b**, Subclustering of myeloid cells/macrophages in single-cell data of human PDAC. Left, cluster analysis based on gene expression (top) or primary tumor versus adjacent tissue (bottom). The dot plot on the right shows the expression of some myeloid genes in the different clusters. Middle, UMAP of the anti-inflammatory gene *MRC1* (CD206) or the pan-myeloid markers *CD14* and *CD163* (left column) and UMAP of *P2RY2*, *P2RY6* and *P2RY14* (right column). Right, dot plot showing *P2RY2*, *P2RY6* and *P2RY14* expression across the different myeloid cell subclusters. *P2RY4* was undetectable. The number of cells analyzed is 6,482. **c**, Left, flow cytometric quantification of *P2Y6* expression ( $\Delta$ MFI, that is,

MFI of *P2Y6* minus MFI of the fluorescence minus one (FMO)) in different cell populations of human PDAC samples. Middle, flow cytometric quantification of *P2Y6* expression ( $\Delta$ MFI *P2Y6*) in paired M1-like (CD206<sup>+</sup>CD204<sup>-</sup>) and M2-like (CD206<sup>+</sup>CD204<sup>+</sup>) TAMs in human PDAC tumors. Right, representative histogram of *P2Y6* expression ( $\Delta$ MFI *P2Y6*) in TAM subsets; Iso, isotype control; % max, each curve was scaled to mode = 100% (ECs and cancer cells,  $n = 3$  (left); all others  $n = 5$ ;  $n = 6$  (right)). **d, e**, Flow cytometric quantification of *P2Y6* expression ( $\Delta$ MFI *P2Y6*) in different cell populations from orthotopic KPC FC1245 (**d**) and s.c. PancO2 (**e**) tumors ( $n = 7$ ). In **c**,  $n$  represents the number of individuals. In **d** and **e**,  $n$  represents the number of biological replicates. Data were analyzed by paired, two-tailed Student's *t*-tests (**c**, middle) and are shown as mean  $\pm$  s.e.m.





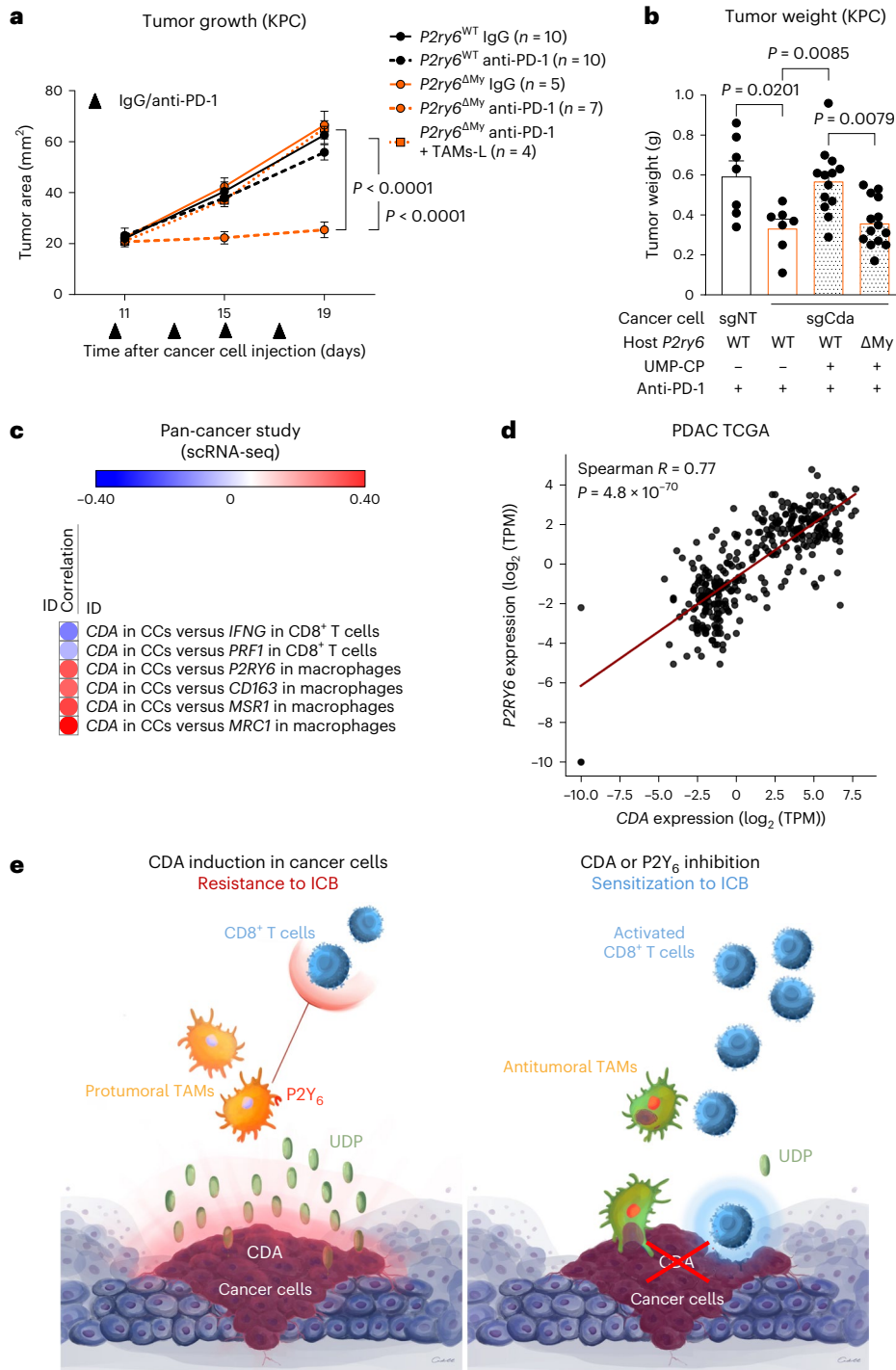


**Fig. 8 | CDA- and UDP-dependent anti-PD-1 resistance is executed by macrophages via the  $P2Y_6$  receptor.** **a**, Longitudinal measurements of tumor area by ultrasound imaging in KPC FC1245 tumor-bearing  $P2y6^{WT}$  and  $P2y6^{\Delta My}$  mice treated with anti-PD-1 or control IgG ( $P2y6^{WT}$  (IgG)  $n = 10$ ,  $P2y6^{WT}$  (anti-PD-1)  $n = 10$ ,  $P2y6^{\Delta My}$  (IgG)  $n = 5$ ,  $P2y6^{\Delta My}$  (anti-PD-1)  $n = 7$ ,  $P2y6^{\Delta My}$  + TAMs-L (anti-PD-1)  $n = 4$ ). Treatment regimen is indicated by the black arrowheads. **b**, Weight of sgNT and sgCda KPC FC1245 tumors in  $P2y6^{WT}$  and  $P2y6^{\Delta My}$  mice treated i.p. with UMP-CP (10 mg per kg (body weight)) or PBS and cotreated with anti-PD-1 (sgNT  $P2y6^{WT}$  (PBS)  $n = 7$ , sgCda  $P2y6^{WT}$  (PBS)  $n = 7$ , sgCda  $P2y6^{WT}$  (UMP-CP)  $n = 13$ , sgCda  $P2y6^{\Delta My}$  (UMP-CP)  $n = 14$ ). Data are representative of a pool of two independent experiments. **c**, Correlation between *CDA* expression in cancer cells (CCs) versus *IFNG* or *PRF1* expression in  $CD8^+$  T cells or *P2RY6*, *CD163*, *MSR1* or *MRC1* expression in macrophages at single-cell resolution in 11 diverse cancer types. **d**, Spearman correlation analysis between *P2RY6* and *CDA* expression in individuals with PDAC from TCGA ( $n = 177$ ); TPM, transcripts per million. **e**, Scheme of the contribution of CDA and  $P2Y_6^+$  macrophages to immunotherapy

resistance. Induction of CDA expression in pancreatic cancer cells contributes to the production and release of uracil nucleotides. Released UDP, as well as UTP-derived UDP, binds with high affinity to the cognate receptor  $P2Y_6$  expressed by TAMs, therefore fostering their recruitment and immunosuppressive features. This ultimately shields the tumor from the entry and activation of cytotoxic T cells, a condition that renders the tumor refractory to anti-PD-1 treatment. Inhibition of CDA or  $P2Y_6$  breaks this cross-talk between cancer cells and TAMs by decreasing the amount of UDP in the TME. It follows that tumors are less infiltrated by immunosuppressive TAMs, and their phenotype is now more immunostimulatory, altogether favoring (instead of preventing) the recruitment and activation of cytotoxic T cells in response to anti-PD-1 treatment. Under this condition, resistant tumors are sensitized to anti-PD-1 therapy, displaying reduced primary growth and metastatic dissemination. In **a** and **b**,  $n$  represents biological replicates. Data were analyzed by two-way repeated measures ANOVA (**a**), two-way ANOVA with a Tukey's multiple comparison test (**b**) and two-sided Spearman's test (**c**). Data are shown as mean  $\pm$  s.e.m.











to classify tumors according to treatment response. For in-house mouse data, we used tumor growth curves to classify tumors into responsive, low-responsive and nonresponsive groups.

We performed differential analysis between responsive and non-responsive tumors on each dataset separately to identify differentially expressed genes and their false discovery rate-corrected *P* values (limma package<sup>74</sup>). We then integrated differential expression results using a product-based meta-analysis<sup>75</sup>. Briefly, we ranked the results of each pairwise comparison by  $\log_2$  (fold change). The most upregulated genes received the lowest rank number (top-ranking genes), and the most downregulated genes received the highest rank number. We combined the rank numbers for all genes in all pairwise comparisons by calculating their product to obtain a final list of ranked genes associated with immunotherapy resistance. To assess statistical significance, we used a recently developed algorithm to determine accurate approximate *P* values for each gene based on the rank product statistic<sup>76</sup> and obtained Benjamini–Hochberg adjusted *P* values using the R package *qvalue*<sup>77</sup>. We filtered rank-based meta-analysis results for metabolic genes, as described previously<sup>78</sup>.

### Human RNA-seq

Various scRNA-seq pan-tumor maps were obtained from Tumor Immune Single Cell Hub<sup>43</sup>. We derived the average expression of *CDA* (in cancer cells only per dataset), *IFNG* or *PRF1* (in CD8<sup>+</sup> T cells only per dataset) or *P2RY6*, *CD163*, *MSRI* or *MRC1* (in macrophages only per dataset) and performed a Pearson's correlation between them using the 16 datasets as variables.

Individuals with PDAC in TCGA were subdivided into two groups, that is, macrophage<sup>high</sup>CD8<sup>+</sup> T cell<sup>low</sup> or macrophage<sup>low</sup>CD8<sup>+</sup> T cell<sup>high</sup> (where macrophages or CD8<sup>+</sup> T cell bifurcations were based on predefined genetic signatures) using established computational workflows, and *CDA* expression in these two subgroups was derived<sup>79,80</sup>. Expression profiles for PDAC samples in  $\log_2(\text{TPM} + 0.001)$  were further processed using Spearman's gene-to-gene correlation with the Python Scipy SpearmanR module<sup>81</sup>.

DESeq2 prenormalized data by the original authors were downloaded from GSE179351. Expression of *PDCDI* and *CDA* in individuals with PDAC before treatment with ICB plus radiotherapy was analyzed and represented as dot plots. Dot sizes represent the proportion of individuals with nonzero expression. The color scale represents standard-scaled mean expression per genetic marker. 'NoResponse' includes individuals that exhibited either stable or progressive disease, whereas 'Response' includes individuals that achieved either partial or complete response, as defined in Supplementary Table 8 of Parikh et al.<sup>22</sup> (NCT03104439).

### FACS analysis on tumors

Mouse tumors were collected and minced in  $\alpha$ MEM (Lonza) supplemented with 5% FBS, 1% Pen/Strep, 50  $\mu$ M  $\beta$ -mercaptoethanol (Gibco), 5 U ml<sup>-1</sup> DNase I (QIAGEN), 0.85 mg ml<sup>-1</sup> collagenase V (collagenase from *Clostridium histolyticum*; Sigma-Aldrich), 1.25 mg ml<sup>-1</sup> collagenase D (collagenase from *C. histolyticum*; Roche) and 1 mg ml<sup>-1</sup> Dispase II (Gibco) and incubated for 30 min at 37 °C. The digested tissue was filtered using a 70- $\mu$ m-pore strainer, and cells were centrifuged for 5 min at 300g. The samples were resuspended in Red Blood Cell Lysing Buffer Hybri-Max (Sigma-Aldrich) for 30 s, inactivated with FACS buffer (PBS containing 2% FBS and 2 mM EDTA) and centrifuged. The cell pellets were resuspended in FACS buffer and filtered with a 40- $\mu$ m-pore strainer. Cells were resuspended in FACS buffer and, for intracellular measurement of IFN $\gamma$  and GZMB, single-cell suspensions were cultured in RPMI supplemented with 10% FBS, 1% glutamine and 1% Pen/Strep and stimulated with phorbol 12-myristate 13-acetate/ionomycin Cell Stimulation Cocktail (eBioscience, 1:500) in the presence of brefeldin A (BioLegend; 1:1,000) or monensin (eBioscience; 1:1,000) for 4 h at 37 °C. Subsequently, cells were incubated for 15 min at 4 °C with

mouse BD Fc block-purified monoclonal rat anti-mouse CD16/CD32 (BD Pharmingen, 553142) and stained with Fixable viability dye (eBioscience, 65-0866-14) and the following antibodies for 30 min at 4 °C: anti-mouse CD45, CD11b, TCR $\beta$  chain, CD4, CD8, CD69, F4/80, IFN $\gamma$ , GZMB, MHC class II, CD11c, CD206, Ly6G, CD335 (Nkp46), Foxp3, CD25 and P2RY<sub>6</sub>. Cells were washed and analyzed by FACS using an LRSFortessa X-20 (BD Bioscience).

Fresh human PDAC samples were digested with Liberase DL (Sigma-Aldrich, 5401160001), Liberase TL (Sigma-Aldrich, 5401020001) and DNase I (Sigma-Aldrich, D4527) in  $\alpha$ MEM supplemented with 2% FBS. The digestion was performed using a MACS dissociator, following the manufacturer's instructions (Miltenyi Biotec). Tumor samples were then resuspended in FACS buffer and filtered through 70- and 40- $\mu$ m-pore strainers. Subsequently, samples were incubated for 15 min at 4 °C with human Fc receptor binding inhibitor (eBioscience, 14-9161-71) and stained for 30 min at 4 °C with the following anti-human antibodies: CD14, P2RY<sub>6</sub>, CD204, CD11b, CD115, HLA-DR, CD3, CD163, CD206, CD45, CD15, CD31 and CD326. Cells were then washed and analyzed by FACS using an LRSFortessa X-20 (BD Bioscience). FMO controls, unstained control and single-staining or IgG isotype controls were performed to ensure proper gating strategy. Data were collected and analyzed with a BD FACSDiva (v.9.0) and FlowJo software (v.10.8.1), respectively.

### Cell sorting

Panc02 CD90.1 and KPC FC1245-CD90.1 tumors were processed as previously mentioned. After obtaining single-cell suspensions, CD45 enrichment was performed by following the manufacturer's instructions (CD45 MicroBeads, mouse, 130-052-301).

Cells (CD45<sup>+</sup> and CD45<sup>-</sup>) were then incubated for 15 min at 4 °C with mouse BD Fc block-purified monoclonal rat anti-mouse CD16/CD32 (BD Pharmingen, 553142) and stained with Fixable viability dye (eBioscience, 65-0866-14 or 65-0863-18) and the following cocktail of antibodies for 30 min at 4 °C: anti-mouse CD45, CD11b, F4/80, TCR $\beta$  chain, CD90.1, CD90.2, CD31, CD11c and Ly6G. Cells were washed and sorted using a FACSARIA Fusion (BD Biosciences) flow cytometer. Data were collected and analyzed with BD FACSDiva (v.9.0) and FlowJo software (v.10.8.1), respectively. FMO controls, unstained controls and single-staining controls were performed to ensure proper gating. Postsort purity of the gating strategy is included in Supplementary Figs. 1–4.

### Statistics and reproducibility

All statistical analyses were performed using GraphPad Prism 9.5.0 software. Statistical significance was calculated by two-tailed unpaired *t*-test on two experimental conditions or multiple two-tailed unpaired *t*-tests and two-way ANOVA when repeated measures were compared, with *P* < 0.05 considered statistically significant as indicated in each figure legend. The exact *P* values are reported in each figure, except when *P* < 0.0001.

No statistical methods were used to predetermine sample sizes, but our sample sizes are similar to those reported in previous publications for the same type of experiments and readout<sup>70,82,83</sup>. The exact sample sizes are indicated in the figure legends. Independent experiments were pooled and analyzed together whenever possible, as detailed in the figure legends. Where appropriate, Shapiro–Wilk tests were performed to check the distribution of samples. Detection of mathematical outliers was then performed using the Grubbs' test in GraphPad. Animals were excluded only if they died, had to be killed according to protocols approved by the animal experimental committees or when the measurement was not reliable for technical issues (specifically for ultrasound). For in vitro experiments, no data were excluded. For in vivo studies, tumor measurement, treatment and analysis were performed blindly by different researchers to ensure that the studies were run in a blinded manner. Animals were randomized,

with each group receiving mice with similar tumor size or similar body weight. For in vitro studies, randomization and blinding of cell lines was not possible; however, all cell lines were treated identically without prior designation. All graphs show mean values  $\pm$  s.e.m.

### Reporting summary

Further information on research design is available in the Nature Portfolio Reporting Summary linked to this article.

### Data availability

In-house mouse bulk RNA-seq datasets that support the findings of this study have been deposited in the Gene Expression Omnibus under accession number [GSE196790](https://www.ncbi.nlm.nih.gov/geo/query/acc.cgi?acc=GSE196790). Publicly available mouse bulk RNA-seq datasets can be found in refs. [30,38](#) under accession numbers [GSE126722](https://www.ncbi.nlm.nih.gov/geo/query/acc.cgi?acc=GSE126722) and E-MTAB-5032. A publicly available mouse orthotopic KPC scRNA-seq dataset from ref. [11](#) under accession number [GSE129455](https://www.ncbi.nlm.nih.gov/geo/query/acc.cgi?acc=GSE129455) was used. For the meta-analysis, publicly available human metastatic melanoma and renal cancer datasets can be found in refs. [3,5,69](#) under accession numbers [GSE78220](https://www.ncbi.nlm.nih.gov/geo/query/acc.cgi?acc=GSE78220) and [GSE67501](https://www.ncbi.nlm.nih.gov/geo/query/acc.cgi?acc=GSE67501) and in dbGap under accession number [phs000452.v2.p1](https://www.ncbi.nlm.nih.gov/geo/query/acc.cgi?acc=phs000452.v2.p1). The bulk RNA-seq human PDAC data were derived from ref. [22](#) under accession number [GSE179351](https://www.ncbi.nlm.nih.gov/geo/query/acc.cgi?acc=GSE179351) and from the TCGA Research Network. TCGA data were downloaded from the UCSC Xena platform (<http://xena.ucsc.edu/>). scRNA-seq data of human PDAC samples can be found in ref. [21](#) under accession number [GSA CRA001160](https://www.ncbi.nlm.nih.gov/geo/query/acc.cgi?acc=GSA_CRA001160). Various human (stomach adenocarcinoma, skin cutaneous melanoma, pancreatic adenocarcinoma, ovarian cancer, non-small cell lung cancer, liver hepatocellular carcinoma, head and neck squamous cell carcinoma, glioblastoma/glioma, colorectal cancer, cholangiocarcinoma and basal cell carcinoma) scRNA-seq datasets were derived from Tumor Immune Single Cell Hub under accession numbers [GSE134520](https://www.ncbi.nlm.nih.gov/geo/query/acc.cgi?acc=GSE134520), [GSE72056](https://www.ncbi.nlm.nih.gov/geo/query/acc.cgi?acc=GSE72056), [GSE111672](https://www.ncbi.nlm.nih.gov/geo/query/acc.cgi?acc=GSE111672), [CRA001160](https://www.ncbi.nlm.nih.gov/geo/query/acc.cgi?acc=CRA001160), [GSE118828](https://www.ncbi.nlm.nih.gov/geo/query/acc.cgi?acc=GSE118828), [GSE143423](https://www.ncbi.nlm.nih.gov/geo/query/acc.cgi?acc=GSE143423), [GSE127465](https://www.ncbi.nlm.nih.gov/geo/query/acc.cgi?acc=GSE127465), [GSE117570](https://www.ncbi.nlm.nih.gov/geo/query/acc.cgi?acc=GSE117570), E-MTAB-6149, [GSE125449](https://www.ncbi.nlm.nih.gov/geo/query/acc.cgi?acc=GSE125449), [GSE103322](https://www.ncbi.nlm.nih.gov/geo/query/acc.cgi?acc=GSE103322), [GSE141982](https://www.ncbi.nlm.nih.gov/geo/query/acc.cgi?acc=GSE141982), [GSE138794](https://www.ncbi.nlm.nih.gov/geo/query/acc.cgi?acc=GSE138794), [GSE146771](https://www.ncbi.nlm.nih.gov/geo/query/acc.cgi?acc=GSE146771), [GSE125449](https://www.ncbi.nlm.nih.gov/geo/query/acc.cgi?acc=GSE125449) and [GSE123813](https://www.ncbi.nlm.nih.gov/geo/query/acc.cgi?acc=GSE123813). In-house LC–MS (in vitro and in vivo) data have been deposited in Metabolomics Workbench<sup>71</sup> under Study IDs ST003154 and ST002791. Source data are provided with this paper. All other data supporting the findings of this study are available from the corresponding author upon reasonable request.

### Code availability

All code used to analyze data in this study is available on GitHub at <https://github.com/mazzonelab>. All other code supporting the findings of this study are available in the Methods or are available from the corresponding author upon reasonable request.

### References

- Smyth, M. J., Ngiew, S. F., Ribas, A. & Teng, M. W. Combination cancer immunotherapies tailored to the tumour microenvironment. *Nat. Rev. Clin. Oncol.* **13**, 143–158 (2015).
- Abaza, A. et al. Programmed cell death protein 1 (PD-1) and programmed cell death ligand 1 (PD-L1) immunotherapy: a promising breakthrough in cancer therapeutics. *Cureus* **15**, e44582 (2023).
- Van Allen, E. M. et al. Genomic correlates of response to CTLA-4 blockade in metastatic melanoma. *Science* **350**, 207–211 (2015).
- Herbst, R. S. et al. Pembrolizumab versus docetaxel for previously treated, PD-L1-positive, advanced non-small-cell lung cancer (KEYNOTE-010): a randomised controlled trial. *Lancet* **387**, 1540–1550 (2016).
- Ascierto, M. L. et al. The intratumoral balance between metabolic and immunologic gene expression is associated with anti-PD-1 response in patients with renal cell carcinoma. *Cancer Immunol. Res.* **4**, 726–733 (2016).
- Le, D. T. et al. PD-1 blockade in tumors with mismatch-repair deficiency. *N. Engl. J. Med.* **372**, 2509–2520 (2015).
- Royal, R. E. et al. Phase 2 trial of single agent ipilimumab (anti-CTLA-4) for locally advanced or metastatic pancreatic adenocarcinoma. *J. Immunother.* **33**, 828–833 (2010).
- Rawla, P., Sunkara, T. & Gaduputi, V. Epidemiology of pancreatic cancer: global trends, etiology and risk factors. *World J. Oncol.* **10**, 10–27 (2019).
- Kamisawa, T., Wood, L. D., Itoi, T. & Takaori, K. Pancreatic cancer. *Lancet* **388**, 73–85 (2016).
- Mantovani, A., Marchesi, F., Malesci, A., Laghi, L. & Allavena, P. Tumour-associated macrophages as treatment targets in oncology. *Nat. Rev. Clin. Oncol.* **14**, 399–416 (2017).
- Elyada, E. et al. Cross-species single-cell analysis of pancreatic ductal adenocarcinoma reveals antigen-presenting cancer-associated fibroblasts. *Cancer Discov.* **9**, 1102–1123 (2019).
- Le, D. T. et al. Results from a phase IIb, randomized, multicenter study of GVAX pancreas and CRS-207 compared with chemotherapy in adults with previously treated metastatic pancreatic adenocarcinoma (ECLIPSE Study). *Clin. Cancer Res.* **25**, 5493–5502 (2019).
- Byrne, W. L., Mills, K. H. G., Lederer, J. A. & Sullivan, G. C. Targeting regulatory T cells in cancer. *Cancer Res.* **71**, 6915 (2011).
- Beatty, G. L. et al. CD40 agonists alter tumor stroma and show efficacy against pancreatic carcinoma in mice and humans. *Science* **331**, 1612–1616 (2011).
- Bader, J. E., Voss, K. & Rathmell, J. C. Targeting metabolism to improve the tumor microenvironment for cancer immunotherapy. *Mol. Cell* **78**, 1019–1033 (2020).
- Zauri, M. et al. CDA directs metabolism of epigenetic nucleosides revealing a therapeutic window in cancer. *Nature* **524**, 114–118 (2015).
- Frese, K. K. et al. Nab-Paclitaxel potentiates gemcitabine activity by reducing cytidine deaminase levels in a mouse model of pancreatic cancer. *Cancer Discov.* **2**, 260–269 (2012).
- Geller, L. T. et al. Potential role of intratumor bacteria in mediating tumor resistance to the chemotherapeutic drug gemcitabine. *Science* **357**, 1156–1160 (2017).
- Weizman, N. et al. Macrophages mediate gemcitabine resistance of pancreatic adenocarcinoma by upregulating cytidine deaminase. *Oncogene* **33**, 3812–3819 (2014).
- Mosteller, F. & Fisher, R. A. Questions and answers: answer to question 14 on combining independent tests of significance. *Am. Stat.* **2**, 30–31 (1948).
- Peng, J. et al. Single-cell RNA-seq highlights intra-tumoral heterogeneity and malignant progression in pancreatic ductal adenocarcinoma. *Cell Res.* **29**, 725–738 (2019).
- Parikh, A. R. et al. Radiation therapy enhances immunotherapy response in microsatellite stable colorectal and pancreatic adenocarcinoma in a phase II trial. *Nat. Cancer* **2**, 1124–1135 (2021).
- Hahn, S. A. et al. DPC4, a candidate tumor suppressor gene at human chromosome 18q21.1. *Science* **271**, 350–353 (1996).
- Hingorani, S. R. et al. *Trp53*<sup>R172H</sup> and *Kras*<sup>G12D</sup> cooperate to promote chromosomal instability and widely metastatic pancreatic ductal adenocarcinoma in mice. *Cancer Cell* **7**, 469–483 (2005).
- Mazzone, M. et al. Heterozygous deficiency of PHD2 restores tumor oxygenation and inhibits metastasis via endothelial normalization. *Cell* **136**, 839–851 (2009).
- Casazza, A. et al. Impeding macrophage entry into hypoxic tumor areas by Sema3A/Nrp1 signaling blockade inhibits angiogenesis and restores antitumor immunity. *Cancer Cell* **24**, 695–709 (2013).
- Ferraris, D. et al. Design, synthesis, and pharmacological evaluation of fluorinated tetrahydropyridine derivatives as inhibitors of cytidine deaminase. *J. Med. Chem.* **57**, 2582–2588 (2014).
- Savona, M. R. et al. An oral fixed-dose combination of decitabine and cedazuridine in myelodysplastic syndromes: a multicentre, open-label, dose-escalation, phase 1 study. *Lancet Haematol.* **6**, e194–e203 (2019).

29. Meeth, K., Wang, J. X., Micevic, G., Damsky, W. & Bosenberg, M. W. The YUMM lines: a series of congenic mouse melanoma cell lines with defined genetic alterations. *Pigment Cell Melanoma Res.* **29**, 590–597 (2016).
30. Wenes, M. et al. Macrophage metabolism controls tumor blood vessel morphogenesis and metastasis. *Cell Metab.* **24**, 701–715 (2016).
31. Kaneda, M. M. et al. PI3K $\gamma$  is a molecular switch that controls immune suppression. *Nature* **539**, 437–442 (2016).
32. Sullivan, M. R. et al. Quantification of microenvironmental metabolites in murine cancers reveals determinants of tumor nutrient availability. *eLife* **8**, e44235 (2019).
33. von Kügelgen, I. Pharmacological profiles of cloned mammalian P2Y-receptor subtypes. *Pharmacol. Ther.* **110**, 415–432 (2006).
34. Nakamura, T., Murata, T., Hori, M. & Ozaki, H. UDP induces intestinal epithelial migration via the P2Y<sub>6</sub> receptor. *Br. J. Pharmacol.* **170**, 883–892 (2013).
35. Abbracchio, M. P. et al. International Union of Pharmacology LVIII: update on the P2Y G protein-coupled nucleotide receptors: from molecular mechanisms and pathophysiology to therapy. *Pharmacol. Rev.* **58**, 281–341 (2006).
36. Communi, D., Piroton, S., Parmentier, M. & Boeynaems, J. M. Cloning and functional expression of a human uridine nucleotide receptor. *J. Biol. Chem.* **270**, 30849–30852 (1995).
37. Chambers, J. K. et al. A G protein-coupled receptor for UDP-glucose. *J. Biol. Chem.* **275**, 10767–10771 (2000).
38. Bieniasz-Krzywiec, P. et al. Podoplanin-expressing macrophages promote lymphangiogenesis and lymphoinvasion in breast cancer. *Cell Metab.* **30**, 917–936 (2019).
39. Nicholas, R. A., Watt, W. C., Lazarowski, E. R., Li, Q. & Harden, K. Uridine nucleotide selectivity of three phospholipase C-activating P2 receptors: identification of a UDP-selective, a UTP-selective, and an ATP- and UTP-specific receptor. *Mol. Pharmacol.* **50**, 224–229 (1996).
40. Koizumi, S. et al. UDP acting at P2Y<sub>6</sub> receptors is a mediator of microglial phagocytosis. *Nature* **446**, 1091–1095 (2007).
41. Zhang, Z. et al. P2Y<sub>6</sub> agonist uridine 5'-diphosphate promotes host defense against bacterial infection via monocyte chemoattractant protein-1-mediated monocytes/macrophages recruitment. *J. Immunol.* **186**, 5376–5387 (2011).
42. von Kügelgen, I. Molecular pharmacology of P2Y receptor subtypes. *Biochem. Pharmacol.* **187**, 114361 (2021).
43. Sun, D. et al. TISCH: a comprehensive web resource enabling interactive single-cell transcriptome visualization of tumor microenvironment. *Nucleic Acids Res.* **49**, D1420–D1430 (2021).
44. Lee, Y. & Biswas, S. K. Rewiring macrophages for anti-tumour immunity. *Nat. Cell Biol.* **18**, 718–720 (2016).
45. Kim, K. et al. Eradication of metastatic mouse cancers resistant to immune checkpoint blockade by suppression of myeloid-derived cells. *Proc. Natl Acad. Sci. USA* **111**, 11774–11779 (2014).
46. Peranzoni, E. et al. Macrophages impede CD8 T cells from reaching tumor cells and limit the efficacy of anti-PD-1 treatment. *Proc. Natl Acad. Sci. USA* **115**, E4041–E4050 (2018).
47. Beumer, J. H. et al. Modulation of gemcitabine (2',2'-difluoro-2'-deoxycytidine) pharmacokinetics, metabolism, and bioavailability in mice by 3,4,5,6-tetrahydrouridine. *Clin. Cancer Res.* **14**, 3529 (2008).
48. Newman, E. M. et al. A phase I, pharmacokinetic, and pharmacodynamic evaluation of the DNA methyltransferase inhibitor 5-fluoro-2'-deoxycytidine, administered with tetrahydrouridine. *Cancer Chemother. Pharmacol.* **75**, 537–546 (2015).
49. Sohal, D. et al. A pilot clinical trial of the cytidine deaminase inhibitor tetrahydrouridine combined with decitabine to target DNMT1 in advanced, chemorefractory pancreatic cancer. *Am. J. Cancer Res.* **10**, 3047–3060 (2020).
50. Eiseman, J. et al. In vivo evaluation of combination treatment with gemcitabine (dFdC) and tetrahydrouridine (THU) in xenograft models of pancreatic cancer. *Cancer Res.* **69**, 4524 (2009).
51. Gravett, A. M., Trautwein, N., Stevanović, S., Dalgleish, A. G. & Copier, J. Gemcitabine alters the proteasome composition and immunopeptidome of tumour cells. *Oncoimmunology* **7**, e1438107 (2018).
52. Zhang, X. et al. Low-dose gemcitabine treatment enhances immunogenicity and natural killer cell-driven tumor immunity in lung cancer. *Front. Immunol.* **11**, 331 (2020).
53. Ito, M. et al. Identification of novel selective P2Y<sub>6</sub> receptor antagonists by high-throughput screening assay. *Life Sci.* **180**, 137–142 (2017).
54. Steculorum, S. M. et al. Inhibition of P2Y<sub>6</sub> signaling in AgRP neurons reduces food intake and improves systemic insulin sensitivity in obesity. *Cell Rep.* **18**, 1587–1597 (2017).
55. Nishida, M. et al. P2Y<sub>6</sub> receptor–G $\alpha_{12/13}$  signalling in cardiomyocytes triggers pressure overload-induced cardiac fibrosis. *EMBO J.* **27**, 3104–3115 (2008).
56. Jain, S. et al. Lack of adipocyte purinergic P2Y. *Proc. Natl Acad. Sci. USA* **117**, 30763–30774 (2020).
57. Nwosu, Z. C. et al. Uridine-derived ribose fuels glucose-restricted pancreatic cancer. *Nature* **618**, 151–158 (2023).
58. Cekic, C. & Linden, J. Purinergic regulation of the immune system. *Nat. Rev. Immunol.* **16**, 177–192 (2016).
59. Allard, B., Beavis, P. A., Darcy, P. K. & Stagg, J. Immunosuppressive activities of adenosine in cancer. *Curr. Opin. Pharmacol.* **29**, 7–16 (2016).
60. Idzko, M. et al. Extracellular ATP triggers and maintains asthmatic airway inflammation by activating dendritic cells. *Nat. Med.* **13**, 913–919 (2007).
61. Mao, C. et al. Impairment of regulatory capacity of CD4<sup>+</sup>CD25<sup>+</sup> regulatory T cells mediated by dendritic cell polarization and hyperthyroidism in Graves' disease. *J. Immunol.* **186**, 4734–4743 (2011).
62. Giannattasio, G. et al. The purinergic G protein-coupled receptor 6 inhibits effector T cell activation in allergic pulmonary inflammation. *J. Immunol.* **187**, 1486–1495 (2011).
63. Qin, J. et al. The UDP/P2Y<sub>6</sub> axis promotes lung metastasis of melanoma by remodeling the premetastatic niche. *Cell. Mol. Immunol.* **17**, 1269–1271 (2020).
64. Giuliani, A. L., Sarti, A. C. & Di Virgilio, F. Extracellular nucleotides and nucleosides as signalling molecules. *Immunol. Lett.* **205**, 16–24 (2019).
65. Kimura, T. et al. Responses of macrophages to the danger signals released from necrotic cells. *Int. Immunol.* **26**, 697–704 (2014).
66. Halbros, C. J. et al. Macrophage-released pyrimidines inhibit gemcitabine therapy in pancreatic cancer. *Cell Metab.* **29**, 1390–1399 (2019).
67. National Comprehensive Cancer Network. *Pancreatic Adenocarcinoma* (version 1.2020) [https://www.nccn.org/professionals/physician\\_gls/pdf/pancreatic.pdf](https://www.nccn.org/professionals/physician_gls/pdf/pancreatic.pdf) (2019).
68. Chen, M. et al. Combined antiangiogenic therapy and immunotherapy is effective for pancreatic cancer with mismatch repair proficiency but high tumor mutation burden: a case report. *Pancreas* **48**, 1232–1236 (2019).
69. Hugo, W. et al. Genomic and transcriptomic features of response to anti-PD-1 therapy in metastatic melanoma. *Cell* **165**, 35–44 (2016).
70. Virga, F. et al. Macrophage miR-210 induction and metabolic reprogramming in response to pathogen interaction boost life-threatening inflammation. *Sci. Adv.* **7**, eabf0466 (2021).
71. Sud, M. et al. Metabolomics Workbench: an international repository for metabolomics data and metadata, metabolite standards, protocols, tutorials and training, and analysis tools. *Nucleic Acids Res.* **44**, D463–D470 (2016).

72. Langmead, B. & Salzberg, S. L. Fast gapped-read alignment with Bowtie 2. *Nat. Methods* **9**, 357–359 (2012).
73. Goveia, J. et al. An integrated gene expression landscape profiling approach to identify lung tumor endothelial cell heterogeneity and angiogenic candidates. *Cancer Cell* **37**, 21–36 (2020).
74. Ritchie, M. E. et al. limma powers differential expression analyses for RNA-sequencing and microarray studies. *Nucleic Acids Res.* **43**, e47 (2015).
75. Hong, F. et al. RankProd: a bioconductor package for detecting differentially expressed genes in meta-analysis. *Bioinformatics* **22**, 2825–2827 (2006).
76. Heskes, T., Eisinga, R. & Breitling, R. A fast algorithm for determining bounds and accurate approximate *P* values of the rank product statistic for replicate experiments. *BMC Bioinformatics* **15**, 367 (2014).
77. Storey, J. D. & Tibshirani, R. Statistical significance for genomewide studies. *Proc. Natl Acad. Sci. USA* **100**, 9440–9445 (2003).
78. Bruning, U. et al. Impairment of angiogenesis by fatty acid synthase inhibition involves mTOR malonylation. *Cell Metab.* **28**, 866–880 (2018).
79. Nagy, Á., Munkácsy, G. & Györfy, B. Pancancer survival analysis of cancer hallmark genes. *Sci. Rep.* **11**, 6047 (2021).
80. Kovács, S. A., Fekete, J. T. & Györfy, B. Predictive biomarkers of immunotherapy response with pharmacological applications in solid tumors. *Acta Pharmacol. Sin.* **44**, 1879–1889 (2023).
81. Virtanen, P. et al. SciPy 1.0: fundamental algorithms for scientific computing in Python. *Nat. Methods* **17**, 261–272 (2020).
82. Celus, W. et al. Plexin-A4 mediates cytotoxic T-cell trafficking and exclusion in cancer. *Cancer Immunol. Res.* **10**, 126–141 (2022).
83. Cappellesso, F. et al. Targeting the bicarbonate transporter SLC4A4 overcomes immunosuppression and immunotherapy resistance in pancreatic cancer. *Nat. Cancer* **3**, 1464–1483 (2022).

## Acknowledgements

T.S. was supported by Fonds Wetenschappelijk Onderzoek (FWO); 11M9922N; Belgium). M. Manco was awarded with a short-term EMBO fellowship (SEG9251; European Molecular Biology Organization) and a 2-year AIRC Post-Doctoral Fellowship for Abroad (ID 28245; Associazione Italiana per la Ricerca sul Cancro). M.P. was supported by Stiftung Deutsche Krebshilfe. R.A. was supported by Fundação para a Ciência e Tecnologia (SFRH/BD/98002/2013). M. Mazzone was funded by a European Research Council Consolidator Grant (ImmunoFit, 773208; European Union) and by FWO (GOA7419N; Belgium). M. Mazzone also received long-term structural Methusalem funding from the Flemish government (METH.14.08). Research in the laboratory of A.D.G. is supported by Research Foundation Flanders (FWO; Fundamental Research grant GOB4620N) and VLIR-UOS (iBOF grant iBOF/21/048, for the 'MIMICRY' consortium). We thank A. Griffa and B. Boeckx for bioinformatic analyses; C. Fuchs for creating the graphical abstract (Fig. 8e); J. Serneels, S. Trusso Cafarello and S. Willox for technical support; the VIB FACS Expertise Center Leuven for flow cytometry measurements; the Metabolomics Core Facility, VIB, for metabolomic measurements and the NIH Common Fund's National Metabolomics Data Repository website and the Metabolomics Workbench, supported by NIH grants U2C-DK119886 and OT2-OD030544.

## Author contributions

T.S., M. Manco, M.P. and R.A. performed all the experiments, data acquisition and interpretation and wrote the manuscript. C.V., F.P., H.H.V.A., R.T. and P.R. performed in vitro assays and tumor experiments. M.V.H., L.W., Y.W., A.A., T.R. and B.T. provided all the clinical samples, stainings, data analysis and pathological interpretation. G.D., A.M.F.C., D.P., S.R., J.F.G., S.-M.F. and B.G. supported with metabolic assays. J.G., A.B. and P.C. performed the meta-analysis. F.P. and E.B. performed stainings and quantifications. J.D. and T.V. performed calcium response experiments. B.M., A.S. and S.S. performed ultrasound imaging and data interpretation. S.N., A.D.G., N.S. and R.D. performed bioinformatic analyses. M.D.M. and A.T. designed and performed all the in vitro gene editing approaches and flow cytometric analyses on human samples. M. Mazzone designed the experiments, analyzed the data, conducted scientific direction and wrote the manuscript.

## Competing interests

The authors declare no conflicts of interest.

## Additional information

**Extended data** is available for this paper at <https://doi.org/10.1038/s43018-024-00771-8>.

**Supplementary information** The online version contains supplementary material available at <https://doi.org/10.1038/s43018-024-00771-8>.

**Correspondence and requests for materials** should be addressed to Massimiliano Mazzone.

**Peer review information** *Nature Cancer* thanks the anonymous reviewers for their contribution to the peer review of this work.

**Reprints and permissions information** is available at [www.nature.com/reprints](http://www.nature.com/reprints).

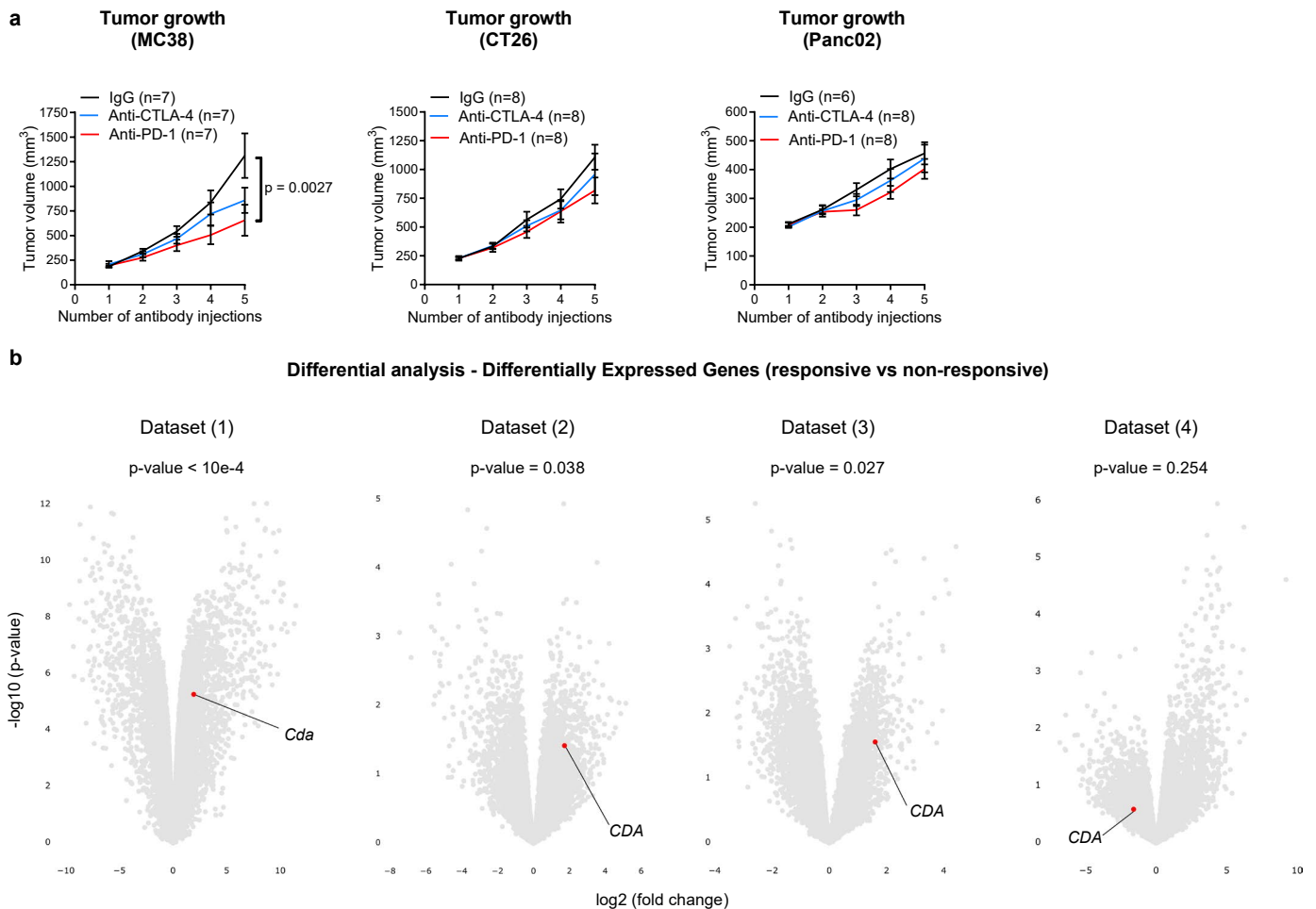
**Publisher's note** Springer Nature remains neutral with regard to jurisdictional claims in published maps and institutional affiliations.

**Open Access** This article is licensed under a Creative Commons Attribution 4.0 International License, which permits use, sharing, adaptation, distribution and reproduction in any medium or format, as long as you give appropriate credit to the original author(s) and the source, provide a link to the Creative Commons licence, and indicate if changes were made. The images or other third party material in this article are included in the article's Creative Commons licence, unless indicated otherwise in a credit line to the material. If material is not included in the article's Creative Commons licence and your intended use is not permitted by statutory regulation or exceeds the permitted use, you will need to obtain permission directly from the copyright holder. To view a copy of this licence, visit <http://creativecommons.org/licenses/by/4.0/>.

© The Author(s) 2024

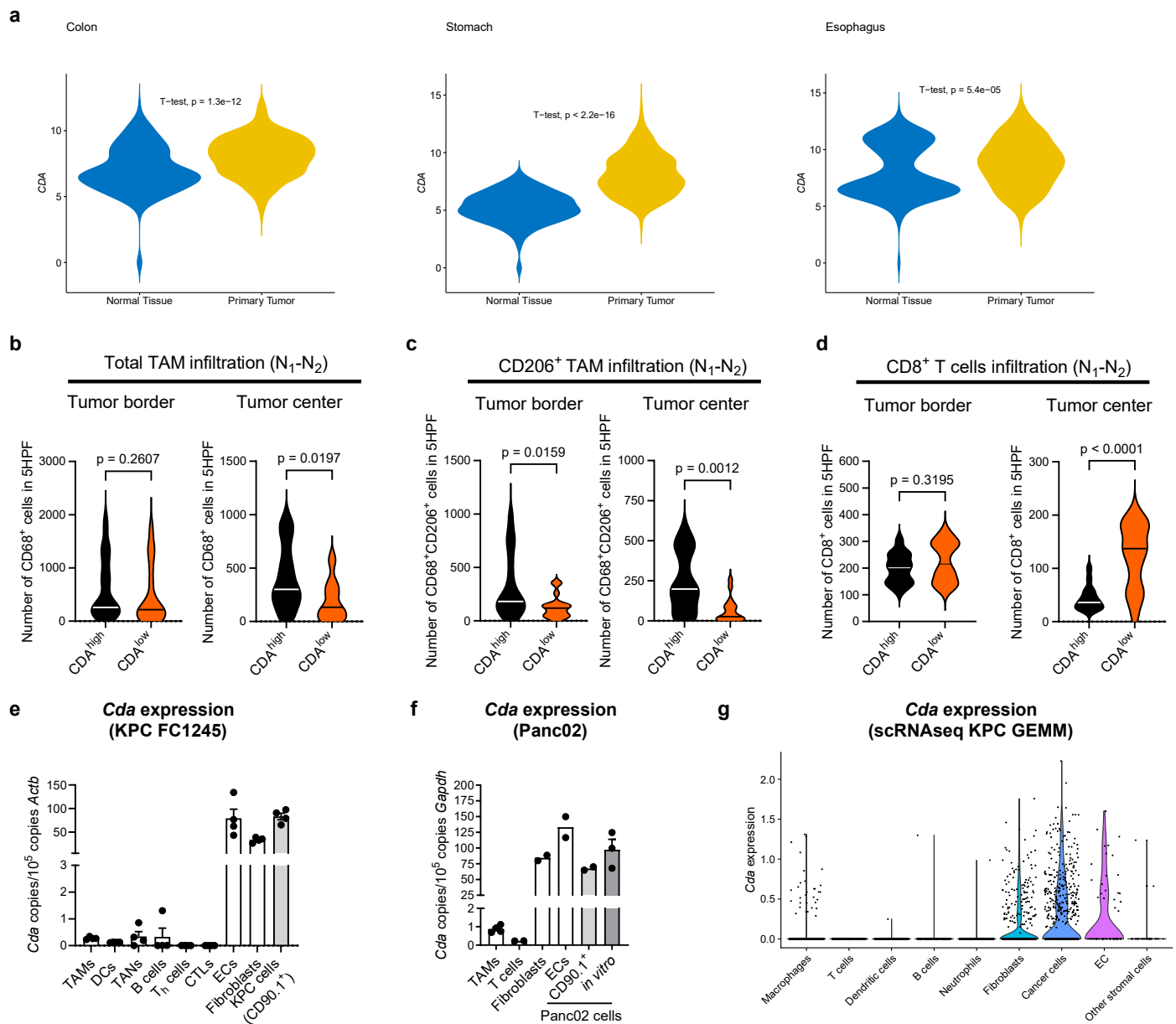
Tommaso Scolaro <sup>1,2,23</sup>, Marta Manco <sup>1,2,23</sup>, Mathieu Pecqueux <sup>1,2,3,23</sup>, Ricardo Amorim <sup>1,2,4,5,23</sup>, Rosa Trotta <sup>1,2</sup>, Heleen H. Van Acker <sup>1,2</sup>, Matthias Van Haele <sup>6</sup>, Niranjana Shirgaonkar <sup>7</sup>, Stefan Naulaerts <sup>8</sup>, Jan Daniluk <sup>9,10</sup>, Fran Prenen <sup>1,2</sup>, Chiara Varamo <sup>1,2</sup>, Donatella Ponti <sup>1,2,11</sup>, Ginevra Doglioni <sup>12,13</sup>, Ana Margarida Ferreira Campos <sup>12,13</sup>, Juan Fernandez Garcia <sup>12,13</sup>, Silvia Radenkovic <sup>14,15</sup>, Pegah Rouhi <sup>1,2</sup>, Aleksandar Beatovic <sup>16</sup>, Liwei Wang <sup>17</sup>, Yu Wang <sup>17</sup>, Amalia Tzoumpa <sup>1,2</sup>, Asier Antoranz <sup>6</sup>, Ara Sargsian <sup>18</sup>, Mario Di Matteo <sup>1,2</sup>, Emanuele Berardi <sup>1,2</sup>, Jermaine Goveia <sup>16,19,20</sup>, Bart Ghesquière <sup>14,15</sup>, Tania Roskams <sup>6</sup>, Stefaan Soenen <sup>21</sup>, Thomas Voets <sup>9,10</sup>, Bella Manshian <sup>18</sup>, Sarah-Maria Fendt <sup>12,13</sup>, Peter Carmeliet <sup>19,20</sup>, Abhishek D. Garg <sup>8</sup>, Ramanuj DasGupta <sup>7</sup>, Baki Topal <sup>22</sup> & Massimiliano Mazzone <sup>1,2</sup> ✉

<sup>1</sup>Laboratory of Tumor Inflammation and Angiogenesis, Center for Cancer Biology, VIB, Leuven, Belgium. <sup>2</sup>Laboratory of Tumor Inflammation and Angiogenesis, Center for Cancer Biology, Department of Oncology, KU Leuven, Leuven, Belgium. <sup>3</sup>Department of Visceral, Thoracic and Vascular Surgery, University Hospital Carl Gustav Carus, Technische Universität Dresden, Dresden, Germany. <sup>4</sup>Life and Health Sciences Research Institute, School of Medicine, University of Minho, Campus de Gualtar, Braga, Portugal. <sup>5</sup>ICVS/3B's-PT Government Associate Laboratory, Braga/Guimarães, Portugal. <sup>6</sup>Department of Imaging and Pathology, Translational Cell and Tissue Research, KU Leuven and University Hospitals Leuven, Leuven, Belgium. <sup>7</sup>Laboratory of Precision Oncology and Cancer Evolution, Genome Institute of Singapore, A\*STAR, Singapore, Singapore. <sup>8</sup>Laboratory for Cell Stress & Immunity (CSI), Department of Cellular & Molecular Medicine, KU Leuven, Leuven, Belgium. <sup>9</sup>Laboratory of Ion Channel Research (LICR), VIB-KU Leuven Centre for Brain & Disease Research, Leuven, Belgium. <sup>10</sup>Department of Cellular and Molecular Medicine, KU Leuven, Leuven, Belgium. <sup>11</sup>Department of Medical-Surgical Sciences and Biotechnologies, University of Rome Sapienza, Latina, Italy. <sup>12</sup>Laboratory of Cellular Metabolism and Metabolic Regulation, Center for Cancer Biology, VIB, Leuven, Belgium. <sup>13</sup>Laboratory of Cellular Metabolism and Metabolic Regulation, Department of Oncology, KU Leuven and Leuven Cancer Institute (LKI), Leuven, Belgium. <sup>14</sup>Metabolomics Core Facility, Center for Cancer Biology, VIB, Leuven, Belgium. <sup>15</sup>Metabolomics Core Facility, Center for Cancer Biology, Department of Oncology, KU Leuven, Leuven, Belgium. <sup>16</sup>Unicle Biomedical Data Science, Leuven, Belgium. <sup>17</sup>State Key Laboratory of Oncogenes and Related Genes, Shanghai Cancer Institute, Department of Oncology, Renji Hospital, School of Medicine, Shanghai Jiao Tong University, Shanghai, China. <sup>18</sup>Translation Cell and Tissue Research Unit, Department of Imaging and Pathology, KU Leuven, Leuven, Belgium. <sup>19</sup>Laboratory of Angiogenesis and Vascular Metabolism, Center for Cancer Biology, VIB, Leuven, Belgium. <sup>20</sup>Laboratory of Angiogenesis and Vascular Metabolism, Center for Cancer Biology, Department of Oncology, KU Leuven, Leuven, Belgium. <sup>21</sup>NanoHealth and Optical Imaging Group, Department of Imaging and Pathology, KU Leuven, Leuven, Belgium. <sup>22</sup>Department of Visceral Surgery, KU Leuven and University Hospitals Leuven, Leuven, Belgium. <sup>23</sup>These authors contributed equally: Tommaso Scolaro, Marta Manco, Mathieu Pecqueux, Ricardo Amorim. ✉e-mail: [massimiliano.mazzone@kuleuven.vib.be](mailto:massimiliano.mazzone@kuleuven.vib.be)



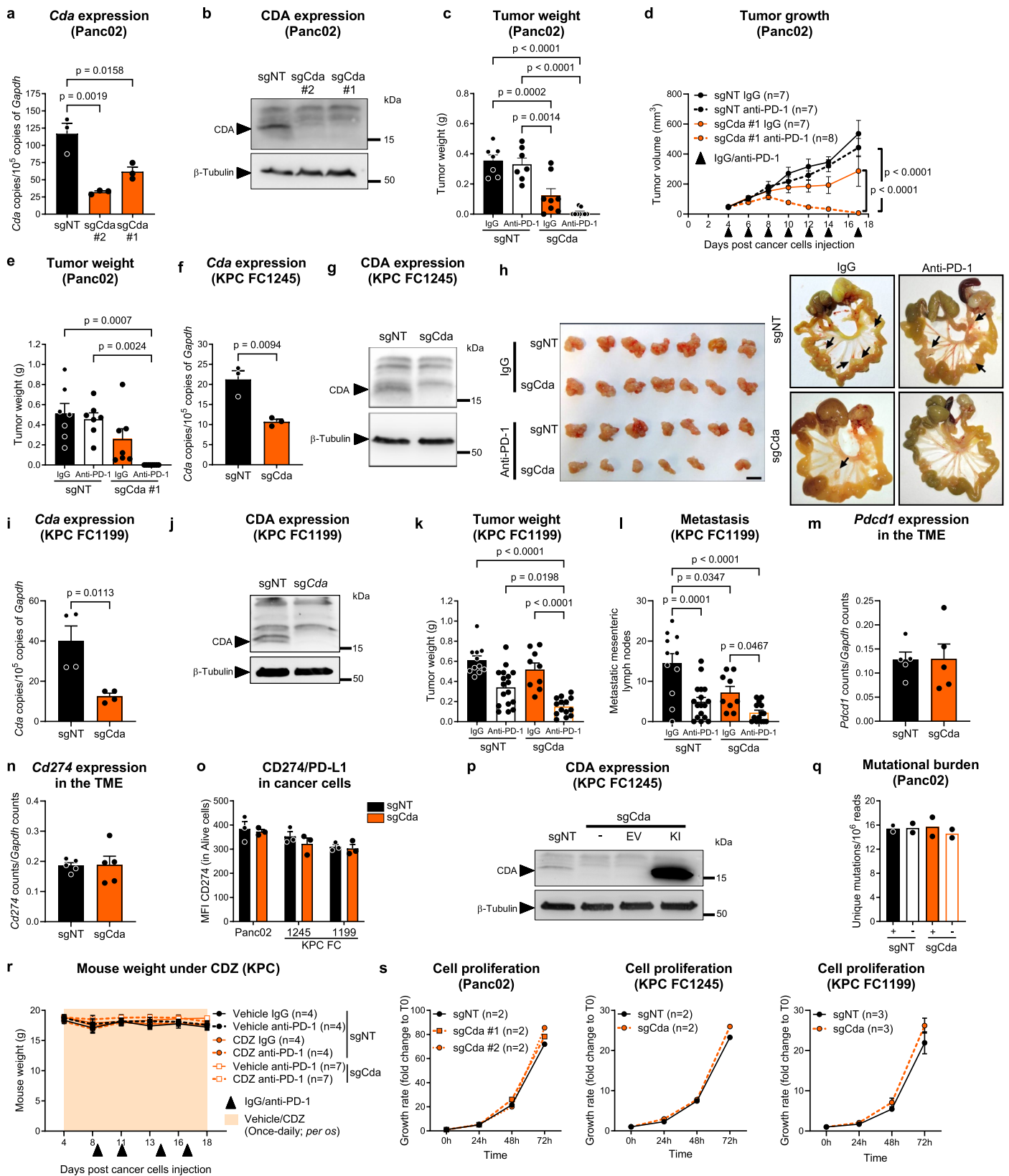
**Extended Data Fig. 1 | Identification of CDA in cancer cells as metabolic player in immunotherapy resistance.** (a) Volume of MC38, CT26 and Panc02 tumors, treated with anti-CTLA-4 (blue), anti-PD-1 (red) or control (CTRL) IgG (black line).  $n=6-8$ .  $n$  represents biological replicates. (b) Volcano plots depicting  $\log_2$  fold change and  $\log_{10}$  (p-value) of differentially expressed genes (*Cda* / *CDA*) indicated in red between responsive and non-responsive tumors, for each of the datasets. From left to right, (1; GSE196790) MC38 vs Panc02; murine; anti-CTLA-4 and

anti-PD-1 treatment;  $\log_2$  fold change = 1.93, p-value <  $1 \times 10^{-4}$ ; (2; GSE78220) metastatic melanoma; human; anti-PD-1 treatment;  $\log_2$  fold change = 1.73, p-value = 0.038; (3; GSE67501) renal cancer; human; anti-PD-1 treatment;  $\log_2$  fold change = 1.60, p-value = 0.027; (4; phs000452.v2.p) metastatic melanoma; human; anti-CTLA-4 treatment;  $\log_2$  fold change = -1.59, p-value = 0.254. Statistical analysis: p value was assessed by two-way RM ANOVA (a), two-sided limma package (b). Graphs show mean  $\pm$  SEM.



**Extended Data Fig. 2 | CDA in cancer cells correlates with immunosuppression.** (a) Violin plot from Xena PanCAN-GTex platform (and selecting for TCGA bulk RNA sequencing datasets only) representing *CDA* expression in colon (Normal Tissue  $n=308$ , Primary Tumor  $n=288$ ), stomach (Normal Tissue  $n=210$ , Primary Tumor  $n=414$ ) and esophagus (Normal Tissue  $n=653$ , Primary Tumor  $n=195$ ) cancer. (b–d) Histological analysis of treatment-naïve, resectable PDAC tumors (out of cohort #1; stage IIb-III; N1-N2). (b) Violin plots of histological quantification of total CD68<sup>+</sup> at tumor border or center. (c) Violin plots of histological quantification of immunosuppressive CD206<sup>+</sup> tumor-associated macrophages (TAMs) at tumor border or center. (d) Violin plots of histological quantification of cytotoxic T cells (CD8<sup>+</sup>) at tumor border

or center. CDA<sup>high</sup>  $n=14$  and CDA<sup>low</sup>  $n=17$  PDAC patients. (e) *Cda* expression in different cell populations sorted from murine orthotopic KPC FC1245 tumors.  $n=4$ .  $n$  represents biological replicates. (f) *Cda* expression in different cell populations sorted from murine s.c. Panc02 tumors (sorted Panc02 CD90.1<sup>+</sup> cells and in vitro Panc02 cells in grey as reference). TAMs  $n=4$ ; in vitro Panc02  $n=3$ ; all the others  $n=2$ .  $n$  represents biological replicates. (g) *Cda* expression in different cell populations in mouse PDAC (KPC GEMM) from a publicly available single-cell RNA-sequencing (scrRNAseq) dataset.  $n=4$ .  $n$  represents biological replicates. Statistical analysis: p value was assessed by unpaired, two-tailed Student's t-test (a, b-d). Graphs show mean  $\pm$  SEM.

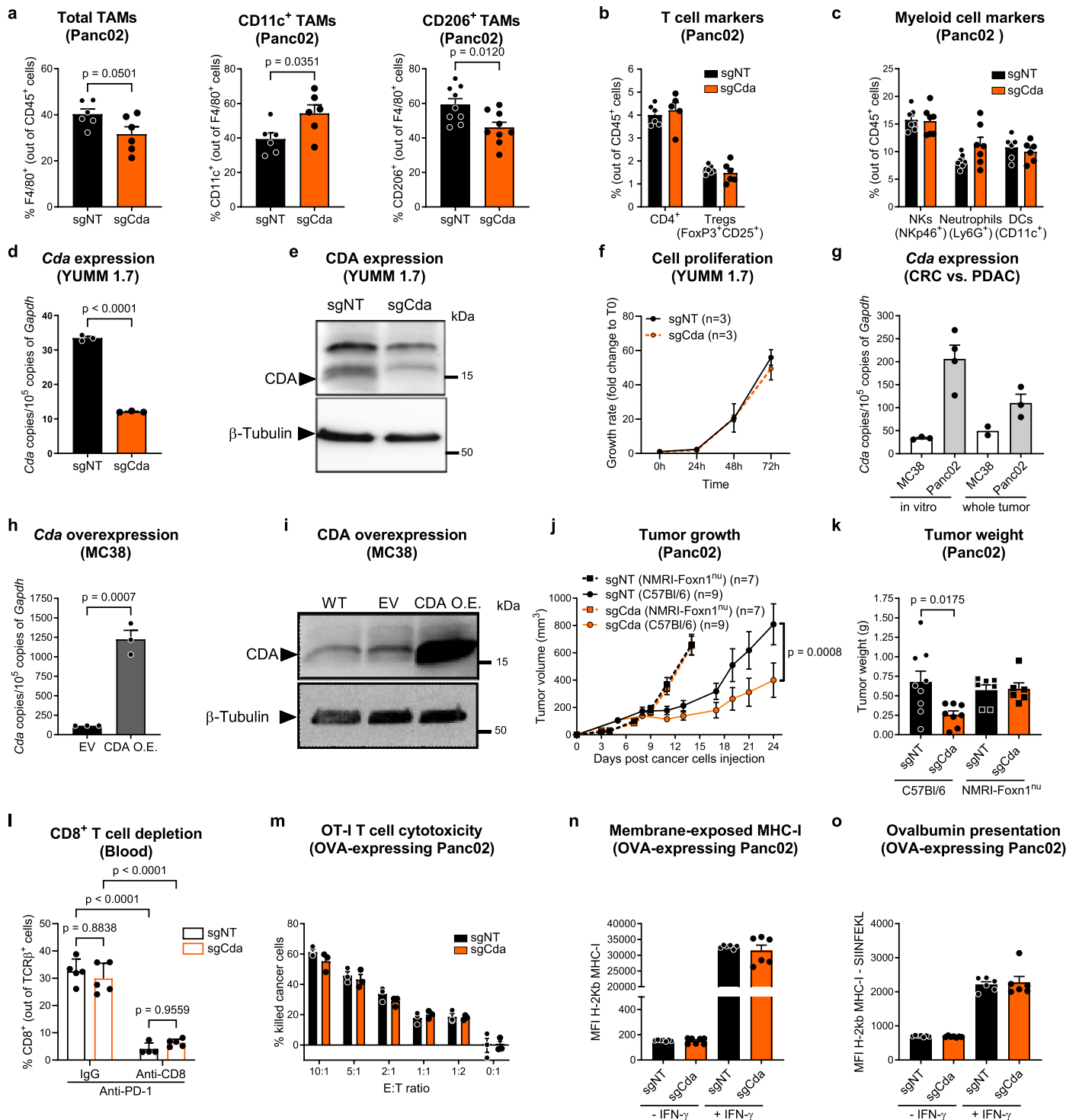


Extended Data Fig. 3 | See next page for caption.



**Extended Data Fig. 3 | Tools' validation for the study of CDA's role in immunotherapy resistance.** (a-b) *Cda* expression in control (sgNT) and sgCda #1 or sgCda #2 (otherwise called sgCda)<sup>Panc02</sup> cells. n=3. n represents independently collected cell seedings. (b) CDA expression in sgNT and sgCda #1 or sgCda #2 Panc02 cells. Representative out of 3 independent experiments. Arrowhead shows CDA specific band. (c-e) (c) Weight of sgNT and sgCda s.c. Panc02 tumors, treated with anti-PD-1 or control IgG. sgNT (IgG) n=7, sgNT (anti-PD-1) n=7, sgCda (IgG) n=8, sgCda (anti-PD-1) n=9. (d-e) Growth and weight of sgNT and sgCda #1 s.c. Panc02 tumors, treated with anti-PD-1 or IgG. Treatment regimen is indicated in (d) by the black arrowheads. sgNT (IgG) n=7, sgNT (anti-PD-1) n=7, sgCda #1 (IgG) n=7, sgCda #1 (anti-PD-1) n=8. n represents biological replicates. (f-g) (f) *Cda* expression in sgNT and sgCda KPC FC1245 cells. n=3. n represents independently collected cell seedings. (g) CDA expression in sgNT and sgCda KPC FC1245 cells. Representative out of 3 independent experiments. Arrowhead shows CDA specific band. (h) Representative images of tumors (left) and metastatic mesenteric lymph nodes (right; arrow) of sgNT and sgCda orthotopic KPC FC1245 tumor-bearing mice, treated with anti-PD-1 or IgG. Scale bar, 1 cm. (i-j) (i) *Cda* expression in sgNT and sgCda KPC FC1199 cells. n=4. n represents independently collected cell seedings. (j) CDA expression in sgNT and sgCda KPC FC1199 cells. Representative out of 3 independent experiments. Arrowhead shows CDA specific band. (k-l) (k) Weight of sgNT and sgCda orthotopic KPC FC1199 tumors, treated with anti-PD-1 or IgG. (l) Quantification of metastatic mesenteric lymph nodes in sgNT and sgCda KPC FC1199 tumor-bearing mice, treated with anti-PD-1 or IgG. (k, l) sgNT (IgG) n=11, sgNT (anti-PD-1)

n=17, sgCda (IgG) n=9, sgCda (anti-PD-1) n=14. n represents biological replicates. Data are representative of a pool of two independent experiments. (m-n) *Pdcd1* and *Cd274* expression in bulk RNAseq from Panc02 sgNT and sgCda tumors. n=5. n represents biological replicates. (o) CD274 expression (MFI in alive cells) in sgNT or sgCda Panc02, KPC FC1245 and KPC FC1199 cells. n=3. n represents independently collected cell seedings. (p) CDA expression in sgNT KPC FC1245, non-transduced (referred to as "-" in the panel), as well as sgCda KPC FC1245 cells transduced with an empty vector (EV) or with a vector overexpressing *Cda* (CDA KI) by Western Blot. Representative out of 3 independent experiments. Arrowhead shows CDA specific band. (q) Mutational burden of Panc02 sgNT and sgCda cells. Cas9 transcription was induced (+) or not (-) with doxycycline (GSE196790). n=2. n represents independently collected cell seedings. (r) Body weight of sgNT or sgCda KPC FC1245 tumor-bearing mice, treated with CDZ/control vehicle, in combination with  $\alpha$ -PD-1 or IgG. Vehicle-sgNT (IgG) n=4, vehicle-sgNT (anti-PD-1) n=4, CDZ-sgNT (IgG) n=4, CDZ-sgNT (anti-PD-1) n=4, vehicle-sgCda (anti-PD-1) n=7 and CDZ-sgCda (anti-PD-1) n=7. Treatment regimen is indicated by the black arrowheads. n represents independently collected cell seedings. Data are representative of a pool of two independent experiments. (s) Cell proliferation of control and *Cda*-depleted Panc02, KPC FC1245 and KPC FC1199 cells. n=2-3. n represents independently collected cell seedings. Statistical analysis: p value was assessed by one-way ANOVA with Tukey's multiple comparison test (a), two-way ANOVA with Tukey's multiple comparison test (c, e, k, l), two-way RM ANOVA (d and s), unpaired, two-tailed Student's t-test (f, i, m, n), multiple unpaired, two-tailed Student's t-test (o). Graphs show mean  $\pm$  SEM.

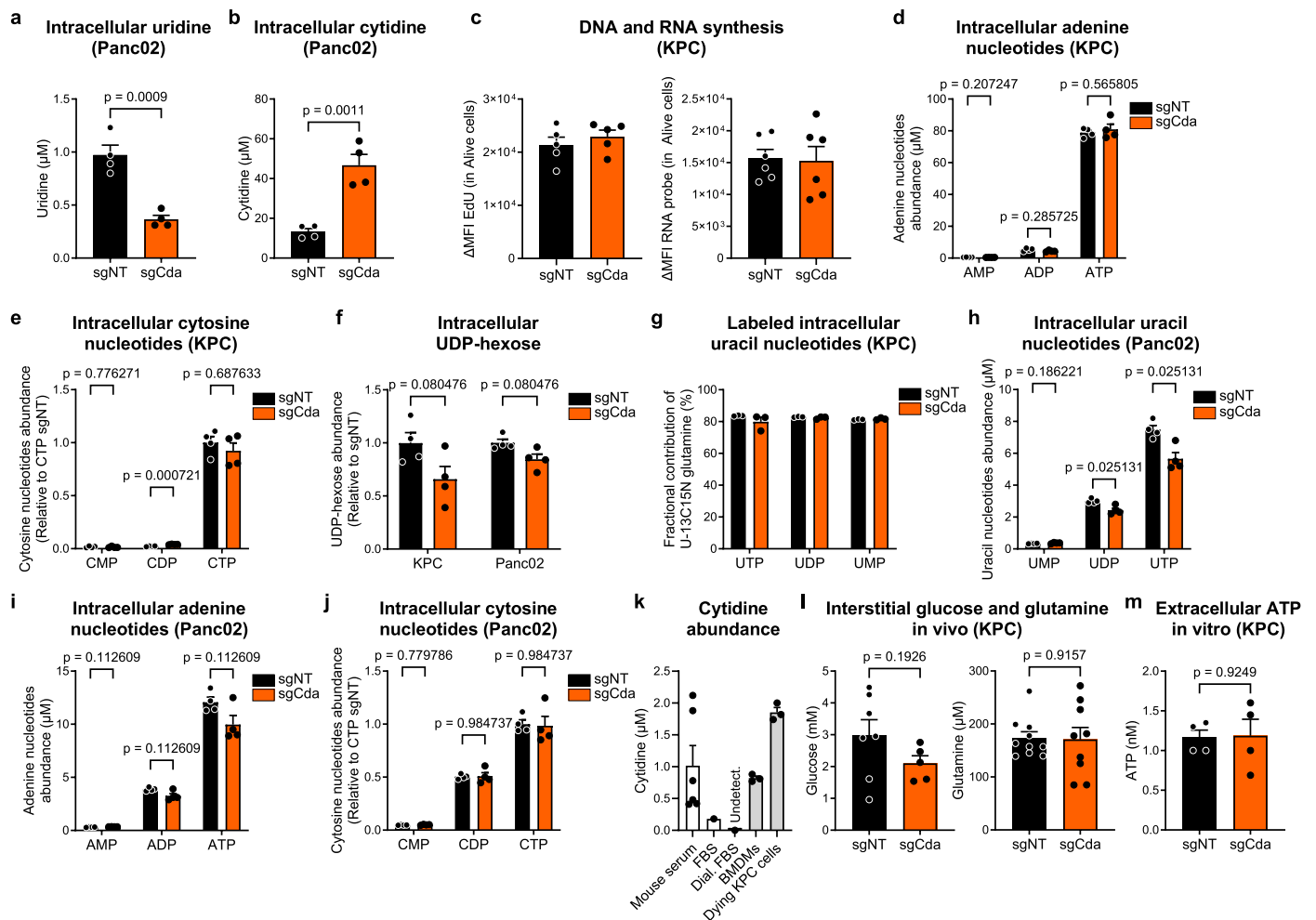


Extended Data Fig. 4 | See next page for caption.

**Extended Data Fig. 4 | CDA inhibition re-shapes the tumor immune**

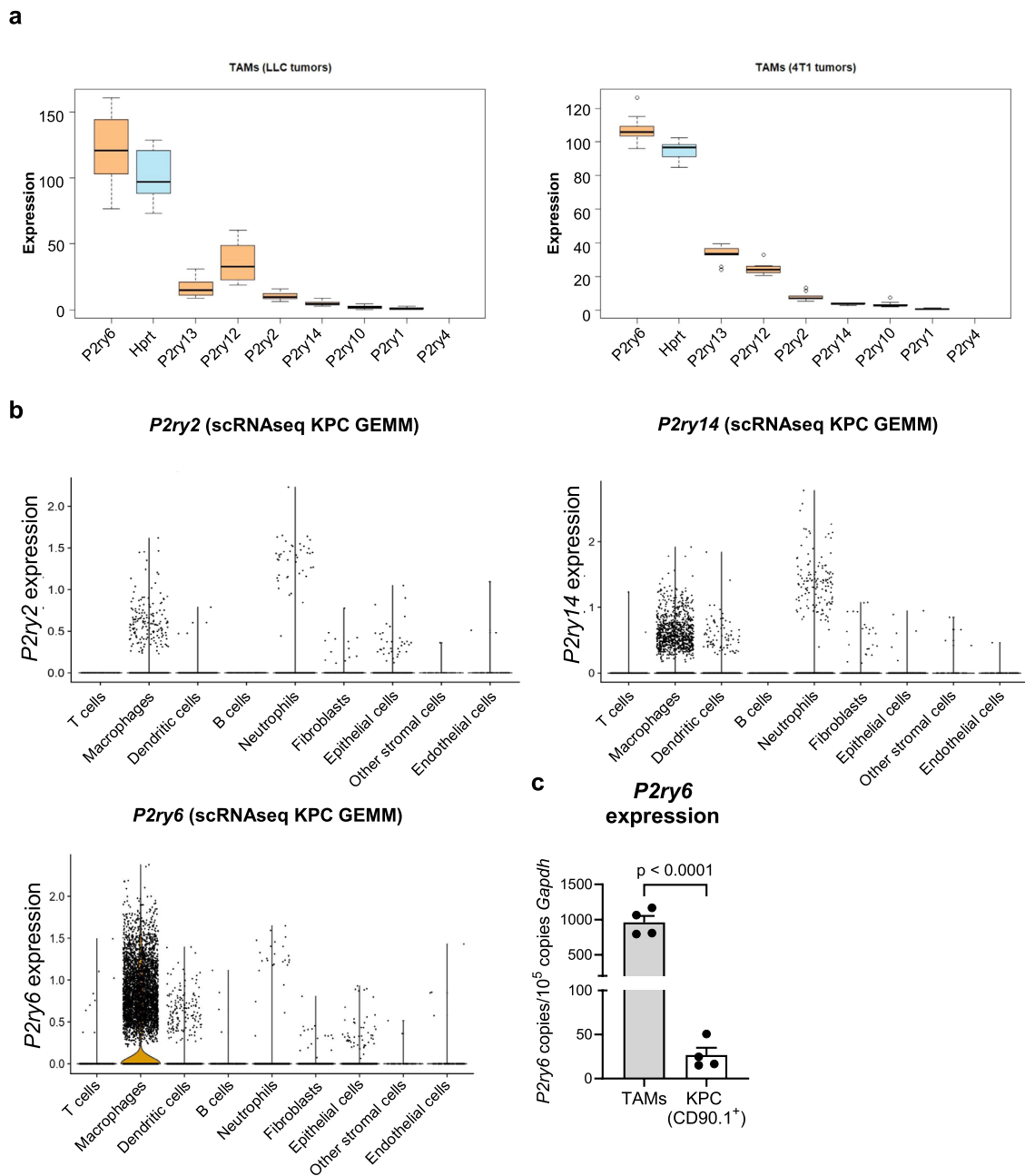
**microenvironment.** (a) Flow cytometric quantification of (left) total (F4/80<sup>+</sup>), (middle) immunostimulatory (CD11c<sup>+</sup>F4/80<sup>+</sup>), and (right) immunosuppressive (CD206<sup>+</sup>F4/80<sup>+</sup>) tumor-associated macrophages (TAMs) in IgG-treated sgNT and sgCda Panc02 tumors. (right) sgNT (n=9) and sgCda (n=9); (left and middle) sgNT (n=6) and sgCda (n=6). n represents biological replicates. (b-c) (b) Flow cytometric quantification of intratumoral helper (CD4<sup>+</sup>) and regulatory (CD4<sup>+</sup>Foxp3<sup>+</sup>CD25<sup>+</sup>) T cells or (c) total natural killer cells (NKp46<sup>+</sup>), neutrophils (Ly6G<sup>+</sup>), dendritic cells (CD11c<sup>+</sup>) in IgG-treated sgNT and sgCda Panc02 tumors. (b) CD4<sup>+</sup>, sgNT (n=7) and sgCda (n=6); Tregs, sgNT (n=6) and sgCda (n=5); (c) DCs, sgNT (n=6) and sgCda (n=6); all the others, sgNT (n=7) and sgCda (n=7). n represents biological replicates. (d-e) (d) *Cda* expression in sgNT and sgCda YUMM1.7 cells. n=3. n represents independently collected cell seedings. (e) CDA expression in sgNT and sgCda YUMM1.7 cells. n represents independently collected cell seedings. Arrowhead shows CDA specific band. (f) Cell proliferation of sgNT and sgCda YUMM1.7 cells. n=3. n represents independently collected cell seedings. (g) *Cda* expression in (left) MC38 and Panc02 cells and (right) whole tumors. MC38 cells n=3; MC38 tumor n=2; Panc02 cells n=4; Panc02 tumor n=3. n represents (in vitro) independently collected cell seedings or (tumor) biological replicates. (h-i) (h) *Cda* expression in MC38 cells transduced with empty vector (EV) or a vector overexpressing *Cda* (CDA O.E). n=3. n represents independently collected cell seedings. (i) CDA expression in non-transduced (referred to as WT), as well as EV or CDA O.E

MC38 cells. n represents independently collected cell seedings. Arrow shows CDA specific band. (j-k) (j) Growth and (k) weight of sgNT and sgCda s.c. Panc02 tumors in nude (NMRI-Fox1nu) or immunocompetent (C57BL/6) mice. (j) sgNT-C57BL/6 n=9, sgCda-C57BL/6 n=9, sgNT-NMRI-Fox1nu n=7, sgCda-NMRI-Fox1nu n=7; (k) sgNT-C57BL/6 n=9, sgCda-C57BL/6 n=8, sgNT-NMRI-Fox1nu n=7, sgCda-NMRI-Fox1nu n=6. n represents biological replicates. Treatment regimen is indicated in (j) by the black arrowheads. (l) Flow cytometric quantification (at end-stage) of cytotoxic T cells (% of CD8<sup>+</sup> out of TCRβ<sup>+</sup> cells) in blood of KPC FC1245 tumor-bearing mice, treated with anti-PD-1 and IgG or anti-CD8 depleting antibody (anti-CD8). sgNT (IgG) n=5, sgCda (IgG) n=5, sgNT (anti-CD8) n=4, sgCda (anti-CD8) n=5. n represents biological replicates. (m) OT-I CD8<sup>+</sup> T-cell killing capacity of sgNT and sgCda OVA-expressing Panc02 cells. n=3. n represents independently collected cell seedings. (n-o) Flow cytometric quantification of (n) total H-2Kb MHC class I and (o) H-2Kb MHC class I bound to the OVA-derived peptide SIINFEKL in OVA-expressing sgNT and sgCda Panc02 cells, at baseline or after IFN-γ stimulation. sgNT (- IFN-γ) n=7, sgCda (- IFN-γ) n=7, sgNT (+ IFN-γ) n=6, sgCda (+ IFN-γ) n=6. n represents independently collected cell seedings. Statistical analysis: p value was assessed by multiple unpaired, two-tailed Student's t-test (a, b, n-o), unpaired, two-tailed Student's t-test (c, d, h), two-way RM ANOVA (f and j), two-way ANOVA with Tukey's multiple comparison test (k), two-way ANOVA with Sidak's multiple comparison test (l, m). Graphs show mean ± SEM.



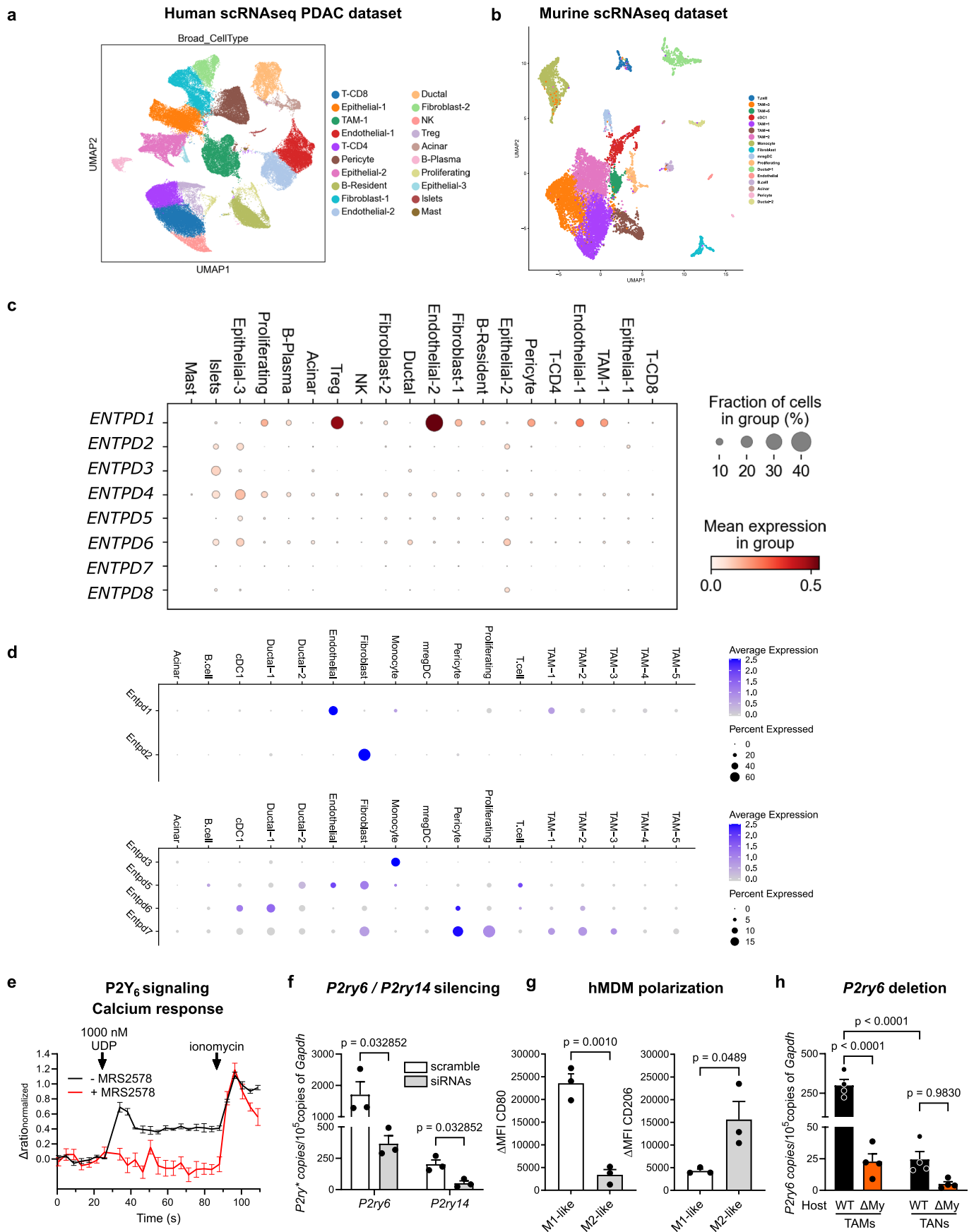
**Extended Data Fig. 5 | Production of various nucleotides and carbon tracing in cancer cells upon CDA depletion.** (a–b) Intracellular abundance of total (a) uridine and (b) cytidine in sgNT and sgCda Panc02 cells. sgNT n=4 and sgCda n=4. (c) DNA and RNA synthesis of sgNT and sgCda KPC FC1245 cells. DNA, n=5; RNA n=6. (d–e) (d) Intracellular levels of adenine (AMP, ADP and ATP) and (e) cytosine (CMP, CDP and CTP) nucleotides in sgNT and sgCda KPC FC1245 cells. sgNT n=4 and sgCda n=4. (f) UDP-hexose species (UDP-glucose and UDP-galactose) in sgNT and sgCda KPC FC1245 and Panc02 cells. sgNT n=4 and sgCda n=4. (g) Fractional contribution (percentage of labelled metabolite out of total amount) of supplemented  $^{13}\text{C}_5, ^{15}\text{N}_2$  glutamine to the intracellular uracil nucleotide pools (UMP, UDP and UTP) in sgNT and sgCda KPC FC1245 cells. sgNT n=3 and sgCda n=3. (h–j) (h) Intracellular levels of uracil nucleotides, (i) adenine nucleotides and (j) cytosine nucleotides in sgNT and sgCda Panc02. sgNT n=4 and sgCda n=4. (k) Extracellular levels of cytidine in mouse serum (tumor-free), standard or dialyzed fetal bovine serum (FBS and Dial. FBS), culture medium of bone marrow-derived macrophages (BMDMs) and (staurosporine-treated) dying KPC FC1245 cancer cells. Mouse serum n=6 (n represents biological replicates),

FBS n=1, Dial. FBS n=1, BMDMs n=3, dying KPC cells n=3. (l) Extracellular levels of (left) glucose and (right) glutamine in the interstitial fluid of orthotopic sgNT and sgCda KPC FC1245 tumors. (left) sgNT n=7 and sgCda n=5; (right) sgNT n=10 and sgCda n=9. (m) Extracellular levels of ATP in the culture medium of sgNT and sgCda KPC FC1245 cells. sgNT n=4 and sgCda n=4. (a–j, l, m) n represents independently collected cell seedings. (a and b, d–l) cytidine, uridine, UDP-hexose, uracil-, adenine- and cytosine-containing nucleotides, glucose, and glutamine were measured by employing liquid chromatography-mass spectrometry. (m) ATP in the culture medium was measured by employing ELISA assay. Cancer cells were cultured in DMEM medium supplemented with 10% dialyzed FBS (to remove the naturally present cytidine) and (a, b, f, h–j) 0.1 mM unlabeled cytidine or (d–f) 0.1 mM  $^{13}\text{C}_5, ^{15}\text{N}_2$  cytidine. (g) KPC FC1245 were cultured in DMEM medium supplemented with 10% dialyzed FBS, 0.1 mM unlabeled cytidine and 2 mM  $^{13}\text{C}_5, ^{15}\text{N}_2$  glutamine. Statistical analysis: p value was assessed by unpaired, two-tailed Student's t-test (a–c, l and m), multiple unpaired Student's t-test (d–j). Graphs show mean  $\pm$  SEM.



**Extended Data Fig. 6 | P2Y receptors in tumor-associated macrophages (TAMs).** (a) Expression of P2Y receptor family members in TAMs of murine (left, E-MTAB-5032) LLC and (right, GSE126722) 4T1 tumors. In box plot, boxes correspond to the 25<sup>th</sup> and 75<sup>th</sup> quartiles, horizontal lines to the median, and whiskers extend to 1.5 times the interquartile range, with outliers shown by dots. LLC n= 16, 4T1 n= 10. (b) (left) *P2ry2*, (middle) *P2ry6* and (right) *P2ry14* expression

in different cell populations in mouse PDAC (KPC GEMM) from a publicly available scRNA-seq dataset (GSE129455). n=4. n represents biological replicates. (c) *P2ry6* expression in TAMs and CD90.1<sup>+</sup> cancer cells sorted from orthotopic KPC FC1245 tumors. n=4. n represents biological replicates. Statistical analysis: p value was assessed by unpaired, two-tailed Student's t-test (c). Graphs show mean  $\pm$  SEM.



Extended Data Fig. 7 | See next page for caption.

**Extended Data Fig. 7 | Expression of ectonucleotidases and P2Y6 in PDAC patients and mouse model.** (a-d) Uniform manifold approximation and projection (UMAP) representing the different cell clusters of PDAC (a) patients or (b) mice, extracted from publicly available scRNAseq datasets (GSA:CRA001160 and GSE129455). Number of cells analyzed is (a) 83960 and (b) 11236. (c-d) Differential expression gene analysis (DEGs) of different ectonucleotidases across the different cell clusters in both PDAC (c) patients and (d) mice. (e) Time course of the changes in the fluorescence ratio (F340/F380) of the calcium indicator Fura-2 in P2ry6<sup>WT</sup> bone marrow-derived macrophages (BMDMs) in response to 1000 nM of UDP with or without MRS2578 (10  $\mu$ M). Responses were normalized to the response to the calcium ionophore ionomycin (2  $\mu$ M). n=3. n represents independently collected cell seedings. (f) *P2ry6* and *P2ry14*

expression in BMDMs after siRNA-mediated silencing by siP2ry6 or siP2ry14 and scramble controls. n=3. n represents independently collected cell seedings. (g) Flow cytometric quantification of CD80 and CD206 expression ( $\Delta$ MFI) in human M1-like (IFN- $\gamma$  + LPS) and M2-like (IL-4) in vitro polarized monocyte-derived macrophages (hMDMs). n=3. n represents independently collected cell seedings. (h) *P2ry6* expression in TAMs and tumor-associated neutrophils (TANs) sorted from orthotopic KPC FC1245 tumors in P2ry6<sup>WT</sup> and P2ry6 <sup>$\Delta$ My</sup> mice. n=4. n represents biological replicates. Statistical analysis: p value was assessed by unpaired, two-tailed Student's t-test (c and f), multiple unpaired, two-tailed Student's t-test (d), two-way ANOVA with Sidak's multiple comparison test (g). Graphs show mean  $\pm$  SEM.

## Reporting Summary

Nature Portfolio wishes to improve the reproducibility of the work that we publish. This form provides structure for consistency and transparency in reporting. For further information on Nature Portfolio policies, see our [Editorial Policies](#) and the [Editorial Policy Checklist](#).

### Statistics

For all statistical analyses, confirm that the following items are present in the figure legend, table legend, main text, or Methods section.

n/a Confirmed

- The exact sample size ( $n$ ) for each experimental group/condition, given as a discrete number and unit of measurement
- A statement on whether measurements were taken from distinct samples or whether the same sample was measured repeatedly
- The statistical test(s) used AND whether they are one- or two-sided  
*Only common tests should be described solely by name; describe more complex techniques in the Methods section.*
- A description of all covariates tested
- A description of any assumptions or corrections, such as tests of normality and adjustment for multiple comparisons
- A full description of the statistical parameters including central tendency (e.g. means) or other basic estimates (e.g. regression coefficient) AND variation (e.g. standard deviation) or associated estimates of uncertainty (e.g. confidence intervals)
- For null hypothesis testing, the test statistic (e.g.  $F$ ,  $t$ ,  $r$ ) with confidence intervals, effect sizes, degrees of freedom and  $P$  value noted  
*Give  $P$  values as exact values whenever suitable.*
- For Bayesian analysis, information on the choice of priors and Markov chain Monte Carlo settings
- For hierarchical and complex designs, identification of the appropriate level for tests and full reporting of outcomes
- Estimates of effect sizes (e.g. Cohen's  $d$ , Pearson's  $r$ ), indicating how they were calculated

*Our web collection on [statistics for biologists](#) contains articles on many of the points above.*

### Software and code

Policy information about [availability of computer code](#)

#### Data collection

Microscopy images were acquired by using Olympus BX41 microscope and CellSense imaging software (v1.18) or Zeiss Axio Scan as indicated in Material and Methods. QuantStudio 12K Flex Real-Time PCR System (Applied Biosystems; v1.4) was used for real-time PCR. Western blot imaging acquisition was performed by using ImageQuant LAS 4000, GE Health Care Life Science Technologies. Flow cytometry data collection was done with BD FACS DIVA software (v9.0). Tumor area by Ultrasound imaging was collected by using Vevo3100 (Vevo LAB 5.7.1) from VisualSonics, Inc. LC-MS analysis was performed by using Q Exactive Hybrid Quadrupole-Orbitrap Mass Spectrometer (Thermo Scientific) or Dionex UltiMate 3000 LC System (Thermo Scientific) as stated in Material and Methods. LC-MS data collection was done using Xcalibur software (Thermo Scientific). Ca<sup>2+</sup> measurement was performed by using Molecular Devices, FlexStation 3.

#### Data analysis

Microscopy images were analyzed by using CellSense imaging software (v1.18). Flow cytometry analysis was performed with the FlowJo software (v10.8.1). Ultrasound images were analyzed using VisualSonics, Inc. imaging software package. LC-MS data analysis was done using Xcalibur software (Thermo Scientific). Bulk-RNAseq reads were mapped to the transcriptome and the mouse reference genome (GRCm38/mm10) using TopHat 2.0 and Bowtie2.0 (Langmead and Salzberg, 2012). Mapped reads were assigned to ensemble gene IDs with the HTSeq software package. Analyses on publicly available murine and human datasets were done using codes mentioned in 'Code availability' section of the manuscript. Statistical analyses on Figure 1b, 1j, 8d and Extended Data Figure 1f were performed in R studio (see 'Code availability'). All other statistical analyses were performed using GraphPad Prism software (v9.5.0).

For manuscripts utilizing custom algorithms or software that are central to the research but not yet described in published literature, software must be made available to editors and reviewers. We strongly encourage code deposition in a community repository (e.g. GitHub). See the Nature Portfolio [guidelines for submitting code & software](#) for further information.



## Data

Policy information about [availability of data](#)

All manuscripts must include a [data availability statement](#). This statement should provide the following information, where applicable:

- Accession codes, unique identifiers, or web links for publicly available datasets
- A description of any restrictions on data availability
- For clinical datasets or third party data, please ensure that the statement adheres to our [policy](#)

In-house murine bulk RNA-seq datasets that support the findings of this study have been deposited in the Gene Expression Omnibus (GEO) under accession no. GSE196790. Publicly available murine bulk RNA-seq datasets can be found in ref.31,39 with accession no. GSE126722 and E-MTAB-5032. Publicly available murine orthotopic KPC scRNA-seq dataset from ref.11 with accession no. GSE129455 was used. For the meta-analysis, human metastatic melanoma and renal cancer publicly available datasets can be found in ref.3,5,20 with accession no. GSE78220, GSE67501 and dbGap, phs000452.v2.p1. The bulk RNA-seq human PDAC data were derived from ref.23 with accession no. GSE179351, and from the TCGA Research Network. TCGA data were downloaded from the UCSC Xena platform (<http://xena.ucsc.edu/>). Single-cell RNA-seq data of human PDAC samples can be found in ref.22 with accession no. GSA CRA001160. Various human (STAD, SKCM, PAAD, OV, NSCLC, LIHC, HNSC, GBM/Glioma, CRC, CHOL, BCC) scRNA-seq datasets were derived from Tumor Immune Single Cell Hub with accession no. GSE134520, GSE72056, GSE111672, CRA001160, GSE118828, GSE143423, GSE127465, GSE117570, EMTAB6149, GSE125449, GSE103322, GSE141982, GSE138794, GSE146771, GSE125449, GSE123813. In-house LC-MS (in vitro and in vivo) data have been deposited in Metabolomics Workbench (ref.71), DATATRACK\_ID:4162 and 4718.

## Human research participants

Policy information about [studies involving human research participants and Sex and Gender in Research](#).

Reporting on sex and gender

As outlined in the method, tumor samples were collected from 63 treatment-naive PDAC patients (31 males and 32 females, referred as cohort #1; UZ KU Leuven Hospital). No gender related issues are applied to this analysis. All clinical data are extensively described in Supplementary Table 1.

Sex/gender of participants were determined on self-report; no transgender participants were present in this study population. Both genders were included and we ruled out the possibility that gender could somehow affect our findings.

Population characteristics

Tumor samples were obtained from naive PDAC patients (referred as cohort #1). All clinical data are extensively described in Supplementary Table 1.

Recruitment

Tumor material was collected either from resected primary tumors during surgery or biopsy. The presence of adenocarcinoma was proven on histopathology.

Ethics oversight

The study was approved by the Ethical Committee of the University Hospitals KU Leuven (Leuven, Belgium) with reference number ML3452 (see Supplementary Table 1). All patients were given informed consent.

Note that full information on the approval of the study protocol must also be provided in the manuscript.

## Field-specific reporting

Please select the one below that is the best fit for your research. If you are not sure, read the appropriate sections before making your selection.

Life sciences  Behavioural & social sciences  Ecological, evolutionary & environmental sciences

For a reference copy of the document with all sections, see [nature.com/documents/nr-reporting-summary-flat.pdf](https://www.nature.com/documents/nr-reporting-summary-flat.pdf)

## Life sciences study design

All studies must disclose on these points even when the disclosure is negative.

Sample size

No statistical methods were used to pre-determine sample sizes but our sample sizes are similar to those reported in previous publications for the same type of experiments and readout (Cappellesso et al. Nature Cancer 2022; Celus et al. Cancer Immunol. Res. 2022; Virga et al. Sci. Adv. 2021). The exact sample sizes are indicated in the figure legends.

Data exclusions

Detection of mathematical outliers was performed using the Grubbs' test in GraphPad after checking (with Shapiro-Wilk test) that our data were normally distributed. Animals were excluded only if they died, had to be killed according to protocols approved by the animal experimental committees, or when the measurement was not reliable for technical issues (specifically for ultrasound). For in vitro experiments no data were excluded.

Replication

Independent experiments were performed in a blinded fashion to assure the reproducibility of the experimental findings. In details, for in vitro experiments three biological replicates were performed with similar results; for in vivo studies at least 4 animals were allocated per group.



CD326 (BD Biosciences, 347198, clone EBA-1, 1:100, RRID: AB\_400262), PE-Cy7 anti-MHC Class I (H-2Kb) (Invitrogen, 25-5958-82, clone AF6-88.5.5.3, 1:200, RRID: AB\_2573505), PE anti-H-2Kb bound to SIINFEKL (BioLegend, 141603, clone 25-D1.16, 1:100, RRID: AB\_10897938).

For in vivo experiments. Rat serum IgG (Sigma-Aldrich, 14131, 10mg/kg); Ultra-LEAF Purified anti-mouse PD-1 (CD279) (BioLegend, 96167, clone RMP1-14, 10mg/kg); InVivoMAb anti-mouse CD8 $\alpha$  (BioCell, BE0004-1, clone 53-6.7, 5 mg/kg).

#### Validation

The antibodies used are established in the field and have been used by a number of groups. RRID was provided in antibody information listed above.

Some antibodies have been additionally validated for use in their respective application.

For Western Blot (anti-mouse CDA). KO cells for CDA were used as negative controls. Overexpressing cells for CDA were used as positive controls.

For histology and immunostainings. As negative control, one section per slide was stained following the same protocol and omitting the primary antibody.

For flow cytometric analysis and FACS. FMO (fluorescence minus one) and isotype controls were evaluated for each antibody to assess specificity in all the stainings.

## Eukaryotic cell lines

Policy information about [cell lines and Sex and Gender in Research](#)

#### Cell line source(s)

The murine pancreatic ductal adenocarcinoma Panc02 cell line was kindly provided by Prof. B. Wiedenmann (Charité, Berlin). The murine pancreatic KPC FC1245 and KPC FC1199 cell lines, were generated from the KPC murine model (KrasLSL.G12D/+; p53R172H/+; Pdx1-Cre<sup>tg</sup>/+), and kindly provided by Prof. D. Tuveson (New York, USA). The murine colon carcinoma MC38 cell line was obtained from Kerafast. CT26 murine colon carcinoma cells were purchased from the American Type Culture Collection (ATCC). The melanoma YUMM 1.7 cell line was a kind gift from Prof. R. Marais (Manchester, UK), and was originally obtained from Sigma-Aldrich.

#### Authentication

An internal golden stock of all cell lines was generated and maintained by the lab manager. One thawed, cells were cultured for no more than ten passages in a humidified incubator in 5% CO<sub>2</sub> and 95% air at 37 C. All cell lines were authenticated based on morphological criteria only.

#### Mycoplasma contamination

Cells lines were tested negative for mycoplasma by Plasmotest<sup>®</sup>-Mycoplasma Detection Kit (InvivoGen) within two weeks after thawing.

#### Commonly misidentified lines (See [ICLAC](#) register)

No commonly misidentified cell lines were used.

## Animals and other research organisms

Policy information about [studies involving animals; ARRIVE guidelines](#) recommended for reporting animal research, and [Sex and Gender in Research](#)

#### Laboratory animals

All mice used were females between 8 and 10 weeks old. Mice were maintained under pathogen-free, temperature- and humidity-controlled conditions under a 12/12-h light/dark cycle and received normal chow (ssniff<sup>®</sup> R/M-H). C57BL/6 and NMRI-Foxn1nu, mice were purchased from Envigo. OT-I mice were purchased from Taconic. P2Y6 (P2ry6tm1Jabo, MGI:5304911) floxed mouse line in C57BL/6 background was kindly provided by Prof. Joshua A. Boyce (Boston, USA). P2ry6lox/lox;LysM-Cre transgenic mice were generated by intercrossing P2ry6-floxed mice with myeloid specific LysM-Cre deleter mouse line (B6.129P2-Lyz2tm1(cre)lfo/J, purchased from Jackson Laboratory).

#### Wild animals

No wild animals were used for this study.

#### Reporting on sex

All mice used were females between 8 and 10 weeks old.

#### Field-collected samples

No field-collected samples were used for this study.

#### Ethics oversight

Housing and all experimental animal procedures were approved by the Institutional Animal Care and Research Advisory Committee of the KU Leuven (ECD P226/2017 and P060/2021). Animals were removed from the experiments and killed if any signs of pain and distress were detected or if the tumor volume went beyond 2000mm<sup>3</sup>. The maximal tumor size was not exceeded in any reported studies.

Note that full information on the approval of the study protocol must also be provided in the manuscript.

## Clinical data

Policy information about [clinical studies](#)

All manuscripts should comply with the ICMJE [guidelines for publication of clinical research](#) and a completed [CONSORT checklist](#) must be included with all submissions.

#### Clinical trial registration

We run retrospective analyses on patients already enrolled in registered clinical trial (NCT03104439)

#### Study protocol

All the information related to their study protocol are available at the following link:

Study protocol	<a href="https://www.clinicaltrials.gov/study/NCT03104439?id=NCT03104439&amp;rank=1">https://www.clinicaltrials.gov/study/NCT03104439?id=NCT03104439&amp;rank=1</a>
Data collection	All the information related to the data collection are publicly available in <a href="https://www.ClinicalTrials.gov/">https://www.ClinicalTrials.gov/</a> (NCT03104439). NCT03104439. Patients enrolled between 07/2017 to 12/2018 in Massachusetts General Hospital (MGH) Cancer Center in Boston, MA as stated in <a href="https://www.clinicaltrials.gov/study/NCT03104439?id=NCT03104439&amp;rank=1">https://www.clinicaltrials.gov/study/NCT03104439?id=NCT03104439&amp;rank=1</a> and published in PMID: 35122060.
Outcomes	Ethical approval number: NCT03104439. All primary and secondary outcomes are publicly available in <a href="https://www.clinicaltrials.gov/study/NCT03104439?id=NCT03104439&amp;rank=1">https://www.clinicaltrials.gov/study/NCT03104439?id=NCT03104439&amp;rank=1</a> and published in PMID: 35122060. DESeq2 pre-normalized data by the original authors was downloaded from GSE179351. Expression of PDCD1 and CDA in PDAC patients prior to treatment with ICB plus radiotherapy in responders and non-responders was analysed and represented as dotplots. Dot sizes represent the proportion of patients with non-zero expression. The color scale represents standard-scaled mean expression per genetic marker. 'NoResponse' includes patients achieving either stable or progressive disease (SD/PD); 'Response' includes patients achieving either partial or complete response (PR/CR) as defined in Supplementary Table 8 of reference <sup>23</sup> (NCT03104439).

## Flow Cytometry

### Plots

Confirm that:

- The axis labels state the marker and fluorochrome used (e.g. CD4-FITC).
- The axis scales are clearly visible. Include numbers along axes only for bottom left plot of group (a 'group' is an analysis of identical markers).
- All plots are contour plots with outliers or pseudocolor plots.
- A numerical value for number of cells or percentage (with statistics) is provided.

### Methodology

Sample preparation	Tumor-bearing mice were sacrificed by cervical dislocation. Tumors were harvested and minced in alpha-MEM medium (Lonza) supplemented with 5% FBS, 1% Pen/Strep, 50 $\mu$ M $\beta$ -mercaptoethanol (Gibco), 5 U/ml DNase I (Qiagen), 0.85 mg/ml Collagenase V (Collagenase from Clostridium histolyticum, Sigma-Aldrich), 1.25 mg/ml Collagenase D (Collagenase from Clostridium histolyticum, Roche) and 1 mg/ml Dispase II (Gibco) and incubated for 30 minutes at 37°C. The digested tissue was filtered using a 70 $\mu$ m pore sized mesh strainer and cells were centrifuged 5 minutes at 300 x g. The samples were resuspended in Red Blood Cell Lysing Buffer Hybri-Max™ (Sigma-Aldrich) for 30 seconds, inactivated with FACS buffer (PBS containing 2% FBS and 2 mM EDTA) and centrifuged. The cell pellets were resuspended in FACS buffer and filtered with a 40 $\mu$ m pore sized mesh strainer. Single cell suspension were centrifuged 5 minutes at 300 x g and cell pellet were resuspended in FACS buffer for antibody staining.
Instrument	FACS LRSFortessa X-20 (BD Bioscience, model number 658226R1); FACS Aria Fusion Cell Sorter (BD Bioscience).
Software	Flow cytometry data collection was done with BD FACS DIVA software (v9.0) Flow cytometry analysis was done with the FlowJo software (v10.8.1).
Cell population abundance	We performed post-sort flow cytometric analyses of each sorted cell population demonstrating that the purity exceeded 94% and most importantly reached around 99% in most of them (Supplementary Figure 1-4).
Gating strategy	Cell subsets were gated as follow: within the CD45 positive gate, we defined TAMs as CD45 positive, CD11b positive and F4/80 positive. M1-like TAMs were gated as CD11c positive or MHC-II high, and M2-like TAMs as CD206 positive, out of F4/80 positive. T cells were gated for FSC/SSC, CD45 positive, CD11b negative and TCR $\beta$ positive. T helper (CD4 positive) and cytotoxic (CD8 positive) T cells were gated out of TCR $\beta$ positive. Out of CD4 positive, Tregs were gated for Foxp3 positive, CD25 positive. Out of CD8 positive, activated CD8+ T cells were gated for CD69 positive, IFN- $\gamma$ positive or GZMB positive, proliferating CD8+ T cells were gated for Ki67 positive. Neutrophils were gated for FSC/SSC, CD45 positive, CD11b positive and Ly6G positive, or alternatively, F4/80 negative. NK cells were gated for FSC/SSC, CD45 positive and NKp46 positive. DCs were gated for FSC/SSC, CD45 positive, CD11b positive, F4/80 negative, CD11c positive. B cells were gated for FSC/SSC, CD45 positive, CD11b negative, CD45R positive, or alternatively, TCR $\beta$ negative. Fibroblasts were gated for FSC/SSC, CD45 negative, CD90.1 (congenic marker of cancer cells) negative and CD90.2 positive. Endothelial cells were gated for FSC/SSC, CD45 negative and CD31 positive. Cancer cells were gated for FSC/SSC, CD45 negative and positive for the congenic marker CD90.1 and CD90.2 negative. All the gatings were performed on the viable cell fraction, excluding all the cells positive for the viability dye (eBioscience™ Fixable Viability Dye eFluor™ 506 or eBioscience™ Fixable Viability Dye eFluor™ 450, depending on the panel composition). See Supplementary Figure 5 and 6.

- Tick this box to confirm that a figure exemplifying the gating strategy is provided in the Supplementary Information.